ORNL/TM-2015/479

Light Water Reactor Sustainability Program

Development of a robust modeling tool for radiation-induced segregation in austenitic stainless steels

September 2015

U.S. Department of Energy

Office of Nuclear Energy

DISCLAIMER

This information was prepared as an account of work sponsored by an agency of the U.S. Government. Neither the U.S. Government nor any agency thereof, nor any of their employees, makes any warranty, expressed or implied, or assumes any legal liability or responsibility for the accuracy, completeness, or usefulness, of any information, apparatus, product, or process disclosed, or represents that its use would not infringe privately owned rights. References herein to any specific commercial product, process, or service by trade name, trade mark, manufacturer, or otherwise, does not necessarily constitute or imply its endorsement, recommendation, or favoring by the U.S. Government or any agency thereof. The views and opinions of authors expressed herein do not necessarily state or reflect those of the U.S. Government or any agency thereof.

ORNL/TM-2015/479

Development of a robust modeling tool for radiation-induced segregation in austenitic stainless steels

Ying Yang, Kevin Field, Todd Allen, Jeremy T. Busby

September 2015

Prepared for the
U.S. Department of Energy
Office of Nuclear Energy

Approved for public release; distribution is unlimited

ABSTRACT

Irradiation-assisted stress corrosion cracking (IASCC) of austenitic stainless steels in Light Water Reactor (LWR) components has been linked to changes in grain boundary composition due to irradiation induced segregation (RIS). This work developed a robust RIS modeling tool to account for thermodynamics and kinetics of the atom and defect transportation under combined thermal and radiation conditions. The diffusion flux equations were based on the Perks model formulated through the linear theory of the thermodynamics of irreversible processes. Both cross and non-cross phenomenological diffusion coefficients in the flux equations were considered and correlated to tracer diffusion coefficients through Manning's relation. The preferential atom-vacancy coupling was described by the mobility model, whereas the preferential atom-interstitial coupling was described by the interstitial binding model. The composition dependence of the thermodynamic factor was modeled using the CALPHAD approach. Detailed analysis on the diffusion fluxes near and at grain boundaries of irradiated austenitic stainless steels suggested the dominant diffusion mechanism for chromium and iron is via vacancy, while that for nickel can swing from the vacancy to the interstitial dominant mechanism. The diffusion flux in the vicinity of a grain boundary was found to be greatly influenced by the composition gradient formed from the transient state, leading to the oscillatory behavior of alloy compositions in this region. This work confirms that both vacancy and interstitial diffusion, and segregation itself, have important roles in determining the microchemistry of Fe, Cr, and Ni at irradiated grain boundaries in austenitic stainless steels.

ACKNOWLEDGEMENTS

This work was supported by the U.S. Department of Energy (DOE), Office of Nuclear Energy, Light Water Reactor Sustainability (LWRS) Research and Development Effort, under contract DE-AC05-00OR22725 with UT-Battelle, LLC.

CONTENTS

ABSTRACT iii

ACKNOWLEDGEMENTS v

1. Introduction and motivation 1

2. Theory and Mathematical Equations 3
   - 2.1 Atom and point defect diffusion fluxes in RIS modeling 3
   - 2.2 Partial diffusion coefficient via vacancy and modeling of mobility 5
   - 2.3 Partial diffusion coefficient via interstitials and interstitial binding factor 6
   - 2.4 Thermodynamic factor 7

3. Calculation results and comparison with experimental data 8
   - 3.1 Diffusion coefficient calculated from the CALPHAD mobility models 8
   - 3.2 RIS modeling 9
     - 3.2.1 Literature data used for model benchmarking 9
     - 3.2.2 Preferential atom-vacancy coupling only 10
     - 3.2.3 RIS modeling through preferential atom-vacancy and atom-interstitial coupling 10

4. Discussion 11
   - 4.1 Thermodynamic factor 11
   - 4.2 Evolution of diffusion fluxes 12
   - 4.3 Diffusion Mechanism 14
   - 4.4 Oscillatory behavior in RIS profile 15

5. Conclusions 17

6. References 19

7. Appendix 29
   - 7.1 Comparison between the calculated tracer diffusion coefficient from the current mobility model and the experimental data 29
   - 7.2 Validation of the current model parameters with experimental data [19] that were not used for optimization. 33

FIGURES

Figure 1 Comparison between the calculated RIS profile across the grain boundary and the experimental data [49]. Dashed line: preferential atom-vacancy coupling only and thermodynamic factor of "1"; solid line: both preferential atom-vacancy and atom-interstitial coupling and thermodynamic factor of "1"; dotted line: both preferential atom-vacancy and atom-interstitial coupling and thermodynamic factor as a function of composition. Open symbols represent data from Kevin and solid symbols represent Edwards' data. 23

Figure 2 Calculated binding factors of Fe, Cr, and Ni as a function of distance from a high-angle random grain boundary 24

Figure 3 Calculated thermodynamic factors of Fe, Cr, and Ni as a function of distance from a high-angle random grain boundary 24

Figure 4 Calculated diffusion fluxes of Cr, Fe, and Ni as a function of distance from the grain boundary at different dose levels of 10^{-7}, 10^{-5}, 10^{-3}, 10^{-1} and 10 dpa. The square, circle, and triangle denote the Cr, Fe, and Ni fluxes, respectively. The solid symbol denotes flux through vacancies and the open symbol denotes flux through interstitials. The net flux is denoted by cross open symbols. 26

Figure 5 (a) Partial diffusion coefficient of chromium and (b) concentration of defects at 10^{-7}, 10^{-5}, 10^{-3}, 10^{-1} , 10 dpa. 26

Figure 6 Calculated net diffusion flux of Fe, Cr and Ni showing flip of Fe from enrichment at 10^{-7}~10^{-3} dpa to depletion at 10^{-1}~10 dpa, and flip of Ni from enrichment at 10^{-7} dpa to depletion at 10^{-5} dpa and then from depletion at 10^{-5}~10^{-3} dpa to enrichment at 10^{-1}~10 dpa. 27

Figure 7 Calculated segregation profiles of Fe and Ni showing w-shape at 0.1 dpa. 28

Figure 8 Comparison between the calculated tracer diffusion coefficient of Cr, Fe Ni (solid line: this work; dash line: Jönsson [23]) and experimental data from Rothman et al.[39]. 29

Figure 9 Comparison between the calculated tracer diffusion coefficient of Cr, Fe Ni (solid line: this work; dash line: Jönsson [23]) and experimental data from Perkins et al.[46-47] 30

Figure 10 Comparison between the calculated tracer diffusion coefficient of Fe and Ni (solid line: this work; dash line: Jönsson [23]) and experimental data from Guiraldenq et al.[45]. 30

Figure 11 Comparison between the calculated tracer diffusion coefficient of Cr (solid line: this work; dash line: Jönsson [23]) and experimental data from Million et al.[40] 31

Figure 12 Comparison between the calculated tracer diffusion coefficient of Fe (solid line: this work; dash line: Jönsson [23]) and experimental data from Million et al.[40] 32

Figure 13 Calculated grain boundary concentrations for Ni and Cr as a function of temperature and dose in Fe-20Cr-24Ni (at%) alloy. Thick line denotes the results from this work and thin line the results from the MIK and Perks model [19]. Symbol denotes the AES measurements [19] 33

Figure 14 Calculated grain boundary concentrations for Ni and Cr as a function of temperature and dose in Ni-18Cr-9Ni (at%) alloy. Thick lines denote the results from this work and thin lines the results from the MIK and Perks model [19]. Symbol denotes the AES measurements [19] 34

TABLES

Table 1 Comparison of calculated ratios of diffusion coefficients between this work and those reported in literature 9

Table 2 Input parameters to the RIS model 10

Table 3 The net fluxes of Cr, Fe, and Ni at the first 10 nodes from GB at different dose levels..... 16

1. Introduction and motivation

Austenitic stainless steels are widely used in nuclear reactors because of their good mechanical properties at high temperatures, excellent corrosion resistance, and good fabricability. They are subjected to extensive neutron radiation and thermal aging during normal nuclear reactor operation. The phenomena of radiation-induced segregation (RIS), radiation-enhanced diffusion, and radiation-induced precipitation are commonly observed in irradiated austenitic stainless steels [1-4]. Microstructural and microchemical changes due to the combined radiation and thermal effects can cause material degradation during service. For example, radiation-induced chromium (Cr) depletion, often observed at grain boundaries (GBs), is suspected of being a key variable for irradiation-assisted stress corrosion cracking [3]; and the enrichment of nickel (Ni) and silicon at dislocations and/or Frank loops promotes the formation of the G phase or γ' phase, contributing to irradiation-induced hardening [5]. Of the various radiation-relevant phenomena, RIS has been subjected to extensive experimental study and theoretical modeling because of its technological importance.

RIS occurs primarily for two reasons. First, radiation produces quantities of point defects (vacancies and interstitials) and defect clusters far in excess of equilibrium concentrations [6]. Second, those defects that are mobile and escape from recombination are reincorporated into the crystal structure at dislocations, GBs, and other defect sinks, sustaining continuous fluxes of radiation-induced defects near the sinks. RIS occurs when the fluxes of these defects are preferentially associated with one or all of the alloying elements of a multi-component alloy. RIS modeling describes the segregation kinetics of a system in which the atomic diffusion is not only subjected to an unusual driving force, i.e., the chemical potential gradient of point defects, but also enhanced by the increased local point defect concentrations caused by irradiation.

RIS of concentrated iron (Fe)-Cr-Ni alloys at GBs has been the subject of extensive experimental study [7-15]. Despite different alloy compositions, irradiation conditions, and the measurement uncertainties of experimental capabilities, the segregation of elements always involves an enrichment of Ni and a depletion of Cr at sinks. This phenomenon has been explained by Marwick's Inverse Kirkendall (IK) effect [16], in which atomic fluxes are driven by defect gradients, as opposed to the Kirkendall effect [17]. RIS of concentrated Fe-Cr-Ni alloys has been simulated using the Perks model [18], in which the IK effect is formulated into diffusion flux equations based on the theory of the thermodynamics of irreversible processes (TIP) [16]. The segregation profile calculated from this model is exclusively from preferential atom-vacancy coupling, assuming a neutral contribution from interstitial flux, i.e., no preferential atom-interstitial association. In the Perks model, the migration energy of an atom via a vacancy is constant and is the same for all three elements (Fe, Cr, and Ni); and the preferential coupling between a vacancy and a constituent element is realized through different atom-vacancy jump rates. The diffusion coefficients calculated from the Perks model could not account for their composition-based dependencies. Allen and Was [19] later modified the Perks IK model by incorporating composition-dependent migration energies into the calculation of diffusion coefficients via vacancy, which greatly enhanced the predictive ability of the model for a wider range of alloy compositions and temperatures. While the effective migration energy in the modified IK (MIK) model is described as composition-dependent, other composition-dependent variables, such as the thermodynamic factor and correlation coefficients, are assumed to be constant. Furthermore, the local equilibrium energy used to calculate the effective migration energy is obtained by averaging the cohesive and ordering energy of binary systems. These

simplifications limit the capability of the Perks or the MIK model to fully describe the composition dependence of RIS profiles.

Both the Perks and the MIK models assume no preferential atom-interstitial coupling. The effective migration energies and jumping frequencies of Fe, Cr, and Ni interstitials are assumed to be the same. To account for preferential atom-interstitial coupling, Wiedersich and Lam [14, 20] added an interstitial binding factor into the IK model. This modification allows dumbbell interstitials, instead of being randomly occupied, to be preferentially occupied based on the binding factor and composition. More sophisticated models [21, 22] that derive kinetic equations from the microscopic configurations of interstitial dumbbell complexes were also used to model interstitial diffusion. However, because of a lack of data for interstitial diffusion, other simplifications were needed, such as neglecting the correlation factors.

Oscillatory behavior of RIS profiles, such as a "w-shape" in the vicinity of a GB, was often observed [11, 15]. Busby et al. [11] found that such behavior is related to the thermodynamic segregation due to Gibbsian adsorption before irradiation. They were able to describe the transitory w-shape profile, although the shape disappears at a dose of 0.001 dpa, much earlier than in experimental observations (1 dpa). The discrepancy might be due to the use of a constant thermodynamic factor [6]. Nastar recently used atomistic-scale mean-field lattice rate models to simulate composition-dependent jump frequencies [6]. By using the enriched Cr profile either from experimental measurement or model calculation as input, a w-shape profile was predicted as a transient state toward the strong post-irradiation depletion of Cr. Nastar also attributed the oscillatory behavior in RIS profiles to the local equilibrium between the surface plane and the next plane.

The present work proposes a systematic strategy for evaluating the diffusion flux through both the vacancies and the interstitials in irradiated Fe-Cr-Ni alloys. First, composition-dependent mobility models for Fe, Cr, and Ni are developed using the CALPHAD (CALculation of PHAse Diagram) approach [23, 24]. The CALPHAD approach has been widely used to model the Gibbs free energy and diffusion activation energy/prefactor of alloy phases as a function of composition and temperature, based on thermodynamic and mobility models [25, 26]. Thermodynamic models are optimized based on experimental thermodynamic property and phase equilibrium data. Mobility models are optimized based on experimental self-, tracer-, intrinsic- and inter- diffusion coefficients. Correlation factors are implicitly included in the mobility models. The mobility models developed from the CALPHAD approach are based solely on thermal diffusion data via vacancy, as the high formation energy of the most stable self-interstitial (001) dumbbell in face-centered-cubic (fcc) metals, 3.2~3.6 eV, is large enough to preclude the formation of thermal interstitials [27]. Therefore, CALPHAD mobility models account for preferential atom-vacancy coupling only.

Second, the mobility models are integrated into the RIS model to calculate diffusion fluxes and 1-dimensional segregation profiles at random high-angle GBs. The calculated RIS profiles essentially result from preferential atom-vacancy coupling only, as no preferential atom-interstitial coupling is considered in this step. Third, if the calculated segregation profiles show good agreement with experimentally determined segregation profiles, then a conclusion can be reached that the RIS is due to the preferential atom-vacancy coupling mechanism. If not, preferential atom-interstitial coupling is included in the RIS modeling.

Although the composition dependence of the diffusion coefficient through interstitials could also be described by a mobility model similar to the one for diffusion through vacancies, the optimization of the model parameters is subject to large uncertainties because there are few available experimental data for interstitial diffusion. Therefore, the interstitial binding model of Wiedersich and Lam [14, 20] is preferred here because it has fewer adjustable parameters. Optimal values for binding energy are obtained when the calculated RIS profiles best reproduce the experimental RIS data. They are also subject to validation by separate experimental RIS data that are not used for optimization. Fourth, the satisfactory RIS model developed in the third step is used to examine the relative importance of the vacancy and interstitial contribution to RIS in Fe-Cr-Ni alloys, as well as the contribution from the composition gradient due to the segregation itself.

In the following sections, the theory and mathematical equations used for RIS modeling, mobility, thermodynamic factor, and interstitial binding are first presented, followed by the calculated results, their comparison with experimental data, and finally, the discussion and conclusions.

2. Theory and Mathematical Equations

2.1 Atom and point defect diffusion fluxes in RIS modeling

Defect production, recombination, and incorporation at sinks such as dislocations and GBs is modeled in the same way as in the Perks [18] and MIK model [19]. Note that the influence of defect sink characteristics such as GB structure is neglected in the following discussion; it is assumed that all sinks act according to perfect sink criteria and hence approximate RIS observed at random high-angle GBs [28]. This approximation was used to simplify the presentation of the model and analysis. The diffusion flux is described based on the linear theory of TIP used in Wolfer's work [29]. Wolfer has derived flux equations for an A-B binary system. Perks et al. [18] extended it into ternary systems with some simplifications, such as negligible thermodynamic factors and constant migration energy for each element. In this work, the flux equations for ternary systems are derived without such simplifications. The major assumptions of this work, which were adopted from Wolfer's work, are summarized thus: (1) diffusion of atoms takes place via vacancy and interstitial mechanisms. Only single vacancies and interstitials are considered. For the latter, an atom migrates as part of the dumbbell interstitial configuration. (2) No coupling exists between vacancy-associated atom fluxes (J_{AV}, J_{BV}, J_{CV}) and interstitial-associated atom fluxes (J_{AI}, J_{BI}, J_{CI}). According to TIP, the fluxes of atoms and point defects are linearly dependent on the gradients of chemical potentials of all elements and defects. The derivation of the atomic flux equations associated with vacancy is described in Eqs. (1) – (3).

$$J_{AV} = -L_{AA}^{V}\nabla(\mu_A - \mu_V) - L_{AB}^{V}\nabla(\mu_B - \mu_V) - L_{AC}^{V}\nabla(\mu_C - \mu_V)\ . \quad (1)$$

$$J_{BV} = -L_{BB}^{V}\nabla(\mu_B - \mu_V) - L_{AB}^{V}\nabla(\mu_A - \mu_V) - L_{BC}^{V}\nabla(\mu_C - \mu_V)\ . \quad (2)$$

$$J_{CV} = -L_{CC}^{V}\nabla(\mu_C - \mu_V) - L_{AC}^{V}\nabla(\mu_A - \mu_V) - L_{BC}^{V}\nabla(\mu_B - \mu_V)\ . \quad (3)$$

$L_{i,j}^{V}$ (i,j=A, B, C) is the phenomenological coefficients. μ_i ($i = A, B, C, V$) is the chemical potential of A, B, C, and vacancies. The driving forces for these fluxes, J_{iV} (i=A, B, C, V), are the chemical potential gradients of atoms and vacancy defects. The chemical potential can be converted into concentrations through Eqs. (4) and (5):

$$\mu_i = \mu_i^0 + kTln(\gamma_i x_i), (i = A, B, C) \; ; \qquad (4)$$

$$\mu_V = kTln\left(\frac{x_V}{x_V^{eq}}\right), \qquad (5)$$

where μ_i^0 is the chemical potential of the atom in a reference state, T is temperature, γ_i is the activity coefficient, x_i is the mole fraction of element A, B or C. x_V is the mole fraction of vacancy in the system, and $x_V^{eq} = \exp(-\frac{G_V^f}{kT})$ is the thermodynamic equilibrium concentrations of vacancies. G_V^f is the formation energy of a thermal vacancy in an A-B-C alloy. Therefore, the chemical potential gradient can be rewritten based on the concentration gradients:

$$\nabla\mu_i = kT\frac{\varphi_i}{x_i}\nabla x_i \; ; \qquad (6)$$

$$\nabla\mu_V = kT(\frac{1}{x_V}\nabla x_V + \sum_{i=A,B,C}\frac{\partial G_V^f}{kT\partial x_i}\nabla x_i) \; , \qquad (7)$$

where φ_i is the thermodynamic factor of element "i" and denoted by $\varphi_i = 1 + \frac{\partial \ln(\gamma_i)}{\partial \ln(x_i)}$, and k is Boltzman's constant. Assuming the formation energy of a vacancy is independent of the composition variation, the second term in Eq. (7) can then be omitted. The total flux of vacancy J_V is related to the partial flux of vacancy J_{AV}, J_{BV}, and J_{CV} by $J_V = -(J_{AV} + J_{BV} + J_{CV})$. By substituting chemical potential gradient with concentration gradient through Eqs. (6) and (7), J_V equates to

$$J_V = kT(L_{AA}^V + L_{AB}^V + L_{AC}^V)\frac{\varphi_A}{x_A}\nabla x_A + kT(L_{AB}^V + L_{BB}^V + L_{BC}^V)\frac{\varphi_B}{x_B}\nabla x_B + kT(L_{AC}^V + L_{BC}^V + L_{CC}^V)\frac{\varphi_C}{x_C}\nabla x_C - kT(L_{AA}^V + L_{BB}^V + L_{CC}^V + 2 * L_{AB}^V + 2 * L_{AC}^V + 2 * L_{BC}^V)\frac{1}{x_V}\nabla x_V \qquad (8)$$

The phenomenological coefficients $L_{i,j}^V$ (i,j=A, B, C) represent the kinetic response of the alloy to a gradient of chemical potential. However, the diffusion coefficients are normally measured against the composition gradient. The L-coefficient can be traced back only if the whole matrix of diffusion coefficients and the thermodynamic factors are known. Obtaining the whole matrix of diffusion coefficients through experiments is not feasible for most alloys. For concentrated alloys, Manning [30] has derived a relationship between L-coefficients and tracer diffusion coefficients based on the random alloy model. It was later found that Manning's relationship can also be obtained without recourse to the random alloy model [31], as long as there is negligible preferential solute-vacancy binding energy. Klaver et al. [27] conducted ab-initio calculations of the atom-vacancy binding energy of dilute Fe-Cr-Ni austenitic alloys. By using the reference state of the antiferromagnetic double layer structure with tetragonal relaxation of the unit cell, they found the Ni-vacancy binding energy is in the range of 0.016~0.056eV for the first nearest neighbor (nn) and −0.011 ~ −0.005eV for the second nn; and the Cr-vacancy binding energy is in the range of −0.091~0.004eV for the first nn and −0.066 ~ −0.004eV for the second nn. These binding energies are negligible compared with the migration energies of Ni through vacancies (0.891~1.179 eV) and Cr through vacancies (0.56~0.844eV). Therefore, Manning's relationship is considered applicable and is used in this study. In fact, Manning's relationship has been successfully used for concentrated Fe-Cr-Ni and Cu-Ni-Fe

alloys [32, 33]. Wolfer [29] applied Manning's relationship to the derivation of the diffusion flux of a binary system. Here we will use it for the ternary system (Eqs. [9] and [10]):

$$L_{ii} = \left({C_i D_i^*}/{kT} \right) \left(1 + {2C_i D_i^*}/{M_0 \sum_n C_n D_n^*} \right) \quad (i,n=A,B,C)\ ; \qquad (9)$$

$$L_{ij} = L_{ji} = \left({2C_i C_j D_i^* D_j^*}/{M_0 kT \sum_n C_n D_n^*} \right) for\ (i \neq j;\ i,j,n = A,B,C)\ , \qquad (10)$$

where C_i, C_j, and C_m are moles of elements and equal to Nx_i, Nx_j, and Nx_n , respectively; N is the total moles of the system; D_i^*, D_j^*, and D_n^* are tracer diffusion coefficients of the elements; M_0 is a numerical constant and is equal to $2f_0/(1-f_0)$; f_0 is the geometric correlation factor defined by the crystal structure. In the case of an fcc crystal, f_0=0.78145 [30]. Substituting Eqs. (9) and (10) into Eq. (8), the following equations can be obtained:

$$J_V = \frac{N}{f_0} D_{AV}^* \varphi_A \nabla x_A + \frac{N}{f_0} D_{BV}^* \varphi_B \nabla x_B + \frac{N}{f_0} D_{CV}^* \varphi_C \nabla x_C - \frac{N}{f_0} (x_A D_{AV}^* + x_B D_{BV}^* + x_C D_{CV}^*) \frac{1}{x_V} \nabla x_V \qquad (11)$$

In contrast to the diffusion coefficient under thermal conditions, the defect concentration under irradiation relies on the irradiation temperature, dose, dose rate, and microstructure features contributing to the sink density and sink strength. To facilitate the incorporation of these irradiation variables into the RIS model through their relationship to x_V, it was preferable to explicitly express the vacancy concentration. Expression $D_{iV}^* = D_{iV} * x_V$ was used, in which D_{iV} was defined as the partial diffusion coefficient of element *i* through vacancy [20]. Then Eq. (11) becomes

$$J_V = \frac{N}{f_0} x_V (D_{AV} \varphi_A \nabla x_A + D_{BV} \varphi_B \nabla x_B + D_{CV} \varphi_C \nabla x_C) - \frac{N}{f_0} (x_A D_{AV} + x_B D_{BV} + x_C D_{CV}) \nabla x_V\ . \qquad (12)$$

Similar derivations can also be obtained for the atomic flux equations associated with interstitials, but they are not shown here, to simplify the presentation. A similar equation can be derived for the interstitial diffusion flux based on Wolfer's work [29]:

$$J_I = -\frac{N}{f_0} x_I (D_{AI} \varphi_A \nabla x_A + D_{BI} \varphi_B \nabla x_B + D_{CI} \varphi_C \nabla x_C) - \frac{N}{f_0} (x_A D_{AI} + x_B D_{BI} + x_C D_{CI}) \nabla x_I\ . \qquad (13)$$

2.2 Partial diffusion coefficient via vacancy and modeling of mobility

To solve the flux Eqs. (12) and (13), we first need to know the partial diffusion coefficient and the thermodynamic factor of each element. The partial diffusion coefficient via vacancy, D_{iV}, is related to the tracer diffusion coefficient D_{iV}^* through $D_{iV} = D_{iV}^*/x_V^{eq}$. It should be noted here that a lower-case "*i*" relates to a chemical species and not interstitials, which are denoted with an upper case "*I*" in Eq. (13). The tracer diffusion coefficient D_{iV}^* is related to the mobility M_i by means of the Einstein relation:

$$D_{iV}^* = RTM_i\ , \qquad (14)$$

where *R* is the gas constant and *T* is temperature. M_i is the atom mobility given by

$$M_i = M_i^0 \exp(\frac{-Q_i}{RT}) \frac{1}{RT}, \quad (15)$$

where Q_i is the activation energy; M_i^0 is the frequency factor given by $M_i^0 = \exp(\Theta_i)$ [23]. Both Θ_i and Q_i depend on the composition and temperature. In the CALPHAD approach, the composition dependency of Θ_i and Q_i is represented by a linear combination of the values at each end point of the composition space in a Redlich-Kister expansion [34]. Using the Fe-Cr-Ni ternary as an example, if the binary interaction is limited to the second order, it is described as

$$\phi_B = x_{Cr}\phi_B^{Cr} + x_{Fe}\phi_B^{Fe} + x_{Ni}\phi_B^{Ni} + x_{Cr}x_{Fe}\left[{}^0\phi_B^{Cr,Fe} + (x_{Cr} - x_{Fe})\,{}^1\phi_B^{Cr,Fe}\right] + x_{Cr}x_{Ni}\left[{}^0\phi_B^{Cr,Ni} + (x_{Cr} - x_{Ni})\,{}^1\phi_B^{Cr,Ni}\right] + x_{Fe}x_{Ni}\left[{}^0\phi_B^{Fe,Ni} + (x_{Fe} - x_{Ni})\,{}^1\phi_B^{Fe,Ni}\right] + x_{Cr}x_{Fe}x_{Ni}\left[x_{Cr}\,{}^{Cr}\phi_B^{Cr,Fe,Ni} + x_{Fe}\,{}^{Fe}\phi_B^{Cr,Fe,Ni} + x_{Ni}\,{}^{Ni}\phi_B^{Cr,Fe,Ni}\right], \quad (16)$$

where ϕ_B represents a composition-dependent property such as Θ_i and Q_i. ϕ_B^i is called an end-member, denoting the activation energy or frequency factor of B in i. For example, for the fcc phase, Q_{Cr}^{Cr} denotes the activation energy for Cr diffusion in the Cr fcc lattice, while Q_{Cr}^{Ni} denotes that of Cr diffusion in the Ni fcc lattice. ${}^0\phi_B^{i,j}$ denotes the first-order binary interaction between i and j, while ${}^1\phi_B^{i,j}$ denotes the second-order interaction. ${}^i\phi_B^{i,j,k}$ represents the ternary interaction in the i-rich region. These end-member and interaction terms contain parameters to be optimized based on experimental data. Each individual ϕ_B parameter on the right hand side of Eq. (16) can be described as a function of temperature if needed. Once the mobility is obtained through the model mentioned above, the partial diffusion coefficient can be calculated from Eq. (17):

$$D_{iV} = \frac{RTM_i}{x_V^{eq}}, \quad (17)$$

where x_V^{eq} is the vacancy concentration at thermal equilibrium.

2.3 Partial diffusion coefficient via interstitials and interstitial binding factor

Under irradiation, interstitials, instead of being formed thermally, are produced as a result of displacement cascades during the radiation damage process. These interstitials could form preferential atom-interstitial couplings, contributing to the difference in the diffusion coefficients of component species. The nonrandom occupation of interstitials by elemental species due to the preferential atom-interstitial association has been accounted for using an interstitial binding model [14, 20]. The partial diffusion coefficient of atom k through interstitial I is

$$\mathrm{D_{nI}} = \frac{1}{6}\mathrm{b_I^2 z_I \nu_n^I}\frac{\mathrm{C_n^I}}{\mathrm{C_n}} \quad (18)$$

where b_I is the jump distance to the nn interstitialcy site, z_I is the interstitialcy site coordination number, ν_n^I is the jump frequency of element n interstitial to a given nn interstitialcy site, and $\frac{C_n^I}{C_n}$ is the fraction of element n in the interstitials. Because of the lack of experimental data, the variables of b_I, z_I and ν_n^I were set the same for the three elements Fe, Cr, and Ni. The parameters for these variables were taken directly from the MIK model [19]. For random occupation of interstitials by atom n, $C_n^I = C_I C_n$, where C_I is the total interstitial concentration. The nonrandom fraction of interstitials occupied by element n due to preferential atom-interstitial association is described by

$$C_n^I = C_I \frac{C_n\, exp\left(E_{n-I}^b / kT\right)}{C_{Fe}\, exp\left(E_{Fe-I}^b / kT\right) + C_{Cr}\, exp\left(E_{Cr-I}^b / kT\right) + C_{Ni}\, exp\left(E_{Ni-I}^b / kT\right)} \tag{19}$$

where E_{n-I}^b (n is Fe, Cr, and Ni) is the binding energy between an interstitial and element n. If E_{n-I}^b is zero or is the same for all elements, then Eq. (19) is reduced to $C_n^I = C_I C_n$, resulting in the same form as that for random occupation of interstitials, and no preferential coupling exists. When it differs among the elements, preferential coupling between interstitials and elements occurs. In this work, a binding factor, β_n, is defined as

$$\beta_n = \frac{\exp\left((E_{n-I}^b - E_{Fe-I}^b)/kT\right)}{C_{Fe} + C_{Cr}\exp\left((E_{Cr-I}^b - E_{Fe-I}^b)/kT\right) + C_{Ni}\exp\left((E_{Ni-I}^b - E_{Fe-I}^b)/kT\right)} \; (n=Fe, Cr, Ni)\,. \tag{20}$$

The difference between the binding energy of an Fe interstitial and that of Cr (or Ni) corresponds to the average energy gained by converting a Cr interstitial (or a Ni interstitial) into an Fe interstitial defined by Lam [14]. The introduction of this factor will not change the total amount of interstitials but will change only the relative fraction of interstitials occupied by element n through the equation $C_n^I = C_I C_n \beta_n$.

2.4 Thermodynamic factor

In the diffusion flux Eq. (12), the remaining unknown variable is the thermodynamic factor. In an ideal solution, the thermodynamic factor equals "1" and the chemical potential gradient is the concentration gradient, so the chemical driving force for diffusion is proportional to the concentration gradient. In a non-ideal solution, the chemical driving force needs to be modified by the thermodynamic factor. In other words, the thermodynamic factor is used to account for the non-ideal contribution of chemical driving force to the diffusion. It is a function of composition and temperature. In a multicomponent alloy system, thermodynamic factor can be calculated from the following equations [35]

$$\varphi_i = \frac{x_i}{RT}\left(\frac{\partial \mu_i}{\partial x_i} - \frac{1}{1-x_i}\sum_{j\neq i} x_j \frac{\partial \mu_i}{\partial x_j}\right)\,. \tag{21}$$

$$\mu_i = G_m + \frac{\partial G_m}{\partial x_i} - \sum_{j\neq i} x_j \frac{\partial G_m}{\partial x_j}\,. \tag{22}$$

G_m is the molar Gibbs energy of a phase as a function of temperature and composition. In this work, a substitutional solution model was used to model the fcc phase in the Fe-Cr-Ni ternary with the Gibbs energy function described by Eq. (23):

$$G_m = x_{Fe}G_{Fe}^0 + x_{Cr}G_{Cr}^0 + x_{Ni}G_{Ni}^0 + RT(x_{Fe}lnx_{Fe} + x_{Cr}lnx_{Cr} + x_{Ni}lnx_{Ni}) + G^{ex} \tag{23}$$

G_i^0 $(i = Fe, Cr, Ni)$ is the Gibbs energies of the pure elements Fe, Cr, and Ni. They were taken from the SGTE pure element database [36]. G^{ex} is the excess energy of a non-ideal solution phase and is described by the Muggianu's equation [37] in the following:

$$G^{ex} = x_{Fe}x_{Cr}\sum_{i=0,1,2} G^i_{Cr,Fe}(x_{Cr} - x_{Fe}) + x_{Fe}x_{Ni}\sum_{i=0,1,2} G^i_{Fe,Ni}(x_{Fe} - x_{Ni})x_{Fe}x_{Cr} + \sum_{i=0,1,2} G^i_{Cr,Ni}(x_{Cr} - x_{Ni}) + x_{Fe}x_{Cr}x_{Ni}(G^0_{Cr,Fe,Ni}x_{Cr} + G^1_{Cr,Fe,Ni}x_{Fe} + G^2_{Cr,Fe,Ni}x_{Ni}) \quad (24)$$

$G^i_{j,n}$ $(i, j, n = 0,1,2)$ represents the binary interaction coefficients, denoting regular, sub-regular and sub-subregular interactions between element j and n. $G^i_{Cr,Fe,Ni}$ $(i = 0,1,2)$ denotes the ternary interaction coefficients in Cr-, Fe-, and Ni-rich corners. There is also a magnetic contribution to the Gibbs energy. Thermodynamic calculations suggest that the magnetic energy has negligible effects on the calculated thermodynamic factors. Therefore, the magnetic term is not included in this study. The published parameters for the Gibbs energy function [38] of the fcc phase in Fe-Cr-Ni are adopted in this work.

3. Calculation results and comparison with experimental data

3.1 Diffusion coefficient calculated from the CALPHAD mobility models

Jönsson carried out CALPHAD modeling of the mobilities of Cr, Fe, and Ni in fcc Fe-Cr-Ni alloys based upon a large amount of experimental diffusivity data [23]. By close examination, it was found that the agreement between the calculated ratios of diffusion coefficients D^*_{Cr}/D^*_{Ni} and D^*_{Fe}/D^*_{Ni} and the experimental ratios needs improvement. Rothman et al. [39] measured tracer diffusion coefficients for three alloys Fe-15Cr-20Ni, Fe-15Cr-45Ni, and Fe-22Cr-45Ni. They found the ratios of the diffusion coefficients D^*_{Cr}/D^*_{Ni} and D^*_{Fe}/D^*_{Ni} in any one alloy do not vary much with temperature within experimental scattering. A similar relationship was reported by Million et al. [40]. These ratios are critical inputs in the Perks and MIK models and have frequently been used at application temperatures (T<400°C) of nuclear power reactors [18, 19] where the diffusion coefficients were not readily measurable through experiments. Jönsson's models, however, cannot reproduce this relationship [23], especially at low temperatures. Therefore, we reoptimized the model parameters. Although most of the experimental data that had been used in Jönsson's work were used in this optimization, those from Eriksson [41], Hancock and Leak [42], and Kale [43] were excluded because of their large inconsistencies with other data sets. The optimization was carried out in the Pandat software package [44]. The optimized mobility model parameters and the comparison between the calculated diffusion coefficients and the selected experimental data sets [39, 40, 45-48] are shown in Appendix I, Figures 1–5. The calculated tracer diffusion coefficients from this work show improved agreement with Rothman's experimental data [39]. A similar improvement in agreement was found with the Perkins data [46, 47]. The currently calculated ratios of D^*_{Cr}/D^*_{Ni} and D^*_{Fe}/D^*_{Ni} increase with the Ni content in the alloy. The effect of Cr on the calculated ratios seems negligible within experimental uncertainties. The calculated ratios in this work generally compare favorably with experimental data and show improved consistency at low temperatures (T<400°C), as shown in Table 1.

Table 1 Comparison of calculated ratios of diffusion coefficients between this work and those reported in literature

Alloy	D^*_{Cr}/D^*_{Ni}					D^*_{Fe}/D^*_{Ni}				
	963–1400°C			320°C		963–1400°C			320°C	
	Rothman	Jönsson	This work	Jönsson	This work	Rothman	Jönsson	This work	Jönsson	This work
15Cr-20Ni	2.55 ±0.57	1.87 ±0.02	2.57 ±0.03	2.17	2.35	1.67 ±0.31	1.06 ±0.09	1.73 ±0.04	0.32	1.46
15Cr-45Ni	2.86 ±0.66	2.70 ±0.32	2.84 ±0.03	0.47	3.05	2.17 ±0.43	2.27 ±0.69	2.11 ±0.01	0.02	2.12
22Cr-45Ni	2.75 ±0.51	2.26 ±0.29	2.76 ±0.07	0.36	2.37	2.04 ±0.26	1.85 ±0.53	2.14 ±0.09	0.02	1.56

The self- and tracer- diffusion coefficients calculated from the CALPHAD model are composition-dependent. As we assumed earlier, the tracer diffusion coefficients from the CALPHAD models describe a mechanism for diffusivity through vacancies only. Therefore, the mechanism for partial diffusion coefficient through vacancies can be calculated by $D_{iV} = D^*_{iV}/x_V^{eq}$. Under irradiation, the point defect concentrations produced by displacement cascades are several orders of magnitude higher than the equilibrium concentrations. The real diffusion coefficient is calculated by the multiplication of D_{iV} and x_V. x_V is determined by the Frenkel-pair damage production mode, recombination rate, and adsorption rate by defect sinks. Therefore, the mechanism of radiation-enhanced diffusion through vacancies can be evaluated through the ratio of the real vacancy concentration produced by radiation to the thermal vacancy concentration at equilibrium.

3.2 RIS modeling

3.2.1 Literature data used for model benchmarking

Primary benchmarking of the RIS model was completed using experimentally determined RIS profiles on a 304 stainless steel with a nominal composition of Fe-18.76% Cr-12.37% Ni-0.94% Mn-0.04% Si-0.04% Mo-0.021% C. This alloy is essentially a Fe-Cr-Ni ternary alloy, as the amount of other alloying elements is negligible; therefore, it is ideal for benchmarking. This 304 alloy, named “HP304L” after the original report [49] or “Heat E” in subsequent reports was solution-annealed before being neutron irradiated in the BOR-60 fast reactor at ~320° at up to 10.2 dpa with an average dose rate of ~8×10^{-7} dpa/s. Details of the irradiation experimental conditions are available in the original report [49]. The experimental data used in this study are from Edwards [49] . Both data sets were measured using scanning transmission electron microscopy/energy-dispersive x-ray spectroscopy. These two data sets are in general agreement with each other, except for those data in the region very close to the GB. The incident electron probe size in Edwards’ work is ~0.5 nm, and that used in Kevin’s work is 1.5~2 nm. Therefore, the data from Edwards were considered to have higher resolution and hence to more closely represent the real boundary compositions. The current RIS modeling uses 0.5 nm beam size for concentration convolution and assumes a nominal specimen thickness of 100 nm, as neither study reported a measured specimen thickness.

3.2.2 Preferential atom-vacancy coupling only

To calculate the RIS due to preferential atom-vacancy coupling only, the calculation of partial diffusion coefficients from the CALPHAD models was seamlessly integrated into the RIS modeling code; the atomic fluxes at each time and spatial step were updated to reflect the change in composition and diffusion coefficients. The formation energy of vacancy G_V^f used to calculate the partial diffusion coefficient is 1.8 eV for Fe-rich austenitic stainless steel, based on Ehrhart's review [50] and recent first-principles calculation results [27]. Note that although preferential atom-interstitial coupling was not considered in this step, the neutral interstitial fluxes were included. Two parameters were necessary to describe the neutral fluxes of interstitials: effective migration energy and jumping frequency. Their values were set as 0.9 eV and 1.5×10^{12} s^{-1}, respectively, as adopted from the MIK model. The boundary conditions at time t were set as $J_{(k=Fe,Cr,Ni)}(d,t)=0$ and $J_{(Va\ or\ i)}(d,t)=0$ at the center of the grain where d is the distance from GB, $J_{(k=Fe,Cr,Ni)}(0,t)=0$ and $\frac{\nabla C_{va\ or\ i}}{\nabla t}(0,t)=0$ at the GB.

Table 2 Input parameters to the RIS model

Symbol	Definition	Values
f_I	Atom-interstitial correlation factor	0.44
υ_I	Interstitial jump frequency	1.5×10^{12} s^{-1}
E_m^I	Interstitial migration energy	0.9 eV
ρ	Dislocation density	1.0×10^{14} m^{-2}
η	Mobile defect production efficiency	1
$E_{Binding}^{Cr-I}$	Interstitial binding energy of element Cr	0.024 eV
$E_{Binding}^{Fe-I}$	Interstitial binding energy of element Fe	0.006 eV
$E_{Binding}^{Ni-I}$	Interstitial binding energy of element Ni	0.002 eV
E_f^{Va}	Formation energy of vacancy	1.8 eV

The dashed lines in Fig. 1 show the calculated RIS profiles of Fe, Cr, and Ni in HP304L irradiated at 320°C for 10.2 dpa, denoted by "Va" indicating preferential atom-vacancy coupling only. The calculated results show that by assuming preferential coupling with vacancies only, the correct trend of elemental segregation at the GB, i.e., Cr and Fe depletion and Ni enrichment, can be predicted. However, the comparison between the calculated and experimental results also suggested that the magnitude of the Ni enrichment and the Fe and Cr depletion is much larger than the average values from experimental measurements. As the diffusion coefficients were obtained from the CALPHAD models, no effort was made to optimize these diffusion coefficients to fit the experimental RIS data. Instead, the discrepancy was primarily considered a result of preferential atom-interstitial coupling.

3.2.3 RIS modeling through preferential atom-vacancy and atom-interstitial coupling

In this section, in addition to the preferential atom-vacancy coupling outlined in the previous section, RIS modeling also included preferential atom-interstitial coupling. To obtain the best agreement with experimental data, the averaging energies required to convert an Fe-interstitial into a Cr-interstitial or a Ni-interstitial are 0.016 eV and −0.01 eV, respectively. The positive sign means the conversion from an Fe-interstitial to a Cr-interstitial is favorable because it

releases energy, and the negative sign means the conversion from an Fe-interstitial to a Ni-interstitial is unfavorable because it absorbs energy. In other words, it is favorable to form more Cr-interstitials, but not Ni-interstitials. The preferential coupling of atoms with interstitials can also be reflected by binding factors whose values versus distance from the GB are plotted as solid lines in Fig. 2. The binding factor of the Cr-interstitial ranges from 1.31 to 1.36, and the ranges of the binding factors of the Fe- and Ni-interstitials are 0.95–0.98 and 0.79–0.82, respectively. Only the binding factor of Cr is greater than one, suggesting positive binding. In contrast, the binding factor of Ni is less than one, suggesting a repelling interaction between Ni and interstitials. The binding factor of Fe is close to one, suggesting that Fe and interstitials have little interaction. This finding is consistent with the ab-initio calculation results by Klaver et al. [27] in which they studied the defect and solute properties in dilute Fe-Cr-Ni austenitic alloys. They found that Ni is repelled from interstitial sites, but Cr shows positive binding to interstitial sites. They also found that Fe shows little interaction with interstitial sites. Barnard et al. [51] also predicted a positive coupling between Cr and interstitials in an ab-initio molecular dynamics simulation of RIS in Ni-Cr alloys. Our findings are consistent with the reported ab-initio results.

The binding factor for each element remains almost constant through the bulk. The more obvious variation in the vicinity of GBs (<5 nm) is due to the drastic composition change in this region. The calculated RIS profiles with consideration of both preferential atom-vacancy and atom-interstitial coupling are plotted as the solid lines in Fig. 1. They are in good agreement with experimental data.

The same set of parameters was then used to evaluate their applicability to other Fe-Cr-Ni alloys. Two alloys Fe-20Cr-24Ni and Ni-18Cr-9Fe were identified for RIS modeling. These two alloys were used because they cover a wide range of compositions from Fe-rich and Ni-rich regions. In addition, these alloys were used to validate the MIK and the Perks model [19]; a comparison could readily be made between the current model and the MIK and Perks models. The calculated temperature and dose dependence of the concentration profile of Cr and Ni across the GB for the Fe-20Cr-24Ni and Ni-18Cr-9Fe alloys are shown in Appendix II, together with their comparison with literature data. The current calculation shows comparable or better agreement with experimental results, compared with previous modeling results. For the Ni-18Cr-9Fe alloy, it was found the currently used formation energy of vacancy, 1.8 eV, is too large to reproduce the temperature dependence. Based on Ehrhart's review [50], the formation energy of vacancy in Fe-rich and Ni-rich alloys decreases from ~2.25 to ~1.25 eV. Furthermore, based on the ab-initio calculation results, Delczeg et al. [52] found that the formation energy of a vacancy in austenitic Fe-Cr-Ni alloys decreases monotonously with Ni. Therefore, it is unreasonable to use the same formation energy for Fe-rich and Ni-rich alloys. The value of 1.4 eV, used in the previous MIK model [19], was then used for the Ni-18Cr-9Fe alloy in this work.

4. Discussion

4.1 Thermodynamic factor

RIS profiles calculated in Section 3.2.1 and 3.2.2 assume a thermodynamic factor of one, i.e., an ideal solution of the Fe-Cr-Ni alloy. In Fig. 1, the RIS profiles that include the modeling of the composition dependence of the thermodynamic factor were also calculated for the case with both preferential atom-vacancy and atom-interstitial coupling. The results are plotted as dotted lines in Fig. 1. The comparison shows enhanced segregation in the vicinity of the GBs (<5 nm)

of the profiles, with a composition dependence of the thermodynamic factor. The calculated thermodynamic factors of Fe, Cr, and Ni versus the distance from GBs are plotted in Fig. 3. Their values are in the range of 1.06~1.1 for Fe, 0.91~1.04 for Cr, and 0.81~0.83 for Ni, suggesting the enhanced diffusion coefficient of Fe but decreased diffusion coefficient of Ni by thermodynamics. The diffusion coefficient of Cr can be increased or decreased by thermodynamics, depending on the composition. The difference between the thermodynamic factors of Cr and of Ni increases with decreasing distance from the GB, which can contribute to a larger diffusivity difference between Cr and Ni. It is also noted that the thermodynamic factors of Fe and Ni in the vicinity of GBs (<1 nm) increase with decreasing distance from GBs. The change corresponds to short-range ordering or clustering for the compositions close to GBs, as determined by the Gibbs energy function of the Fe-Cr-Ni alloys. Despite the presence of some changes and non-ideality in the thermodynamic factors, the deviation from an ideal solution is small compared with other systems such as Fe-Al with a factor of 10 [53] and Ni-Zr with a factor of 33 [54]. Therefore, the current study suggests that approximating the thermodynamic factors of Fe-Cr-Ni alloys as one is reasonable in the MIK model [11, 19].

4.2 Evolution of diffusion fluxes

This section discusses the evolution of the atomic flux through preferential coupling with vacancies and interstitials. The diffusion fluxes were calculated for five levels of dose: 10^{-7}, 10^{-5}, 10^{-3}, 10^{-1}, and 10 dpa, respectively. The dose levels from 10^{-7} to 10^{-1} dpa are the typical regimes where non-steady RIS occurs for Fe-Cr-Ni alloys [55]. At each dose, three types of fluxes for each element were calculated. The first type is the net flux of each element, denoted by J_k_net (k=Fe, Cr, and Ni). The second type is the flux due to preferential atom-interstitial coupling, denoted by DJ_k_Int. DJ_k_Int is the difference between the true flux of interstitials, when preferential atom-interstitial coupling is considered, and the neutral flux of interstitials when there is no such coupling. The third type of flux is that due to preferential atom-vacancy coupling, denoted by DJ_k_Va. It was defined as the difference between the true flux of atom k through a vacancy when preferential atom-vacancy coupling is considered, and the neutral flux of atom k through a vacancy when there is no such coupling. The sum of the flux of one element due to preferential atom-vacancy, and the flux due to atom-interstitial coupling, equals the net flux of that element. The fluxes due to preferential atom-vacancy and atom-interstitial coupling are shown in the left column of Fig. 4. The net fluxes for each element are shown in the right column of Fig. 4. The calculated fluxes at 10^{-7}, 10^{-5}, 10^{-3}, 10^{-1}, and 10 dpa are plotted in sequence from top to bottom. The fluxes are plotted for the right hand side of the GB only. If the flux has a positive sign, it means that the species is diffusing away from the GB; if it is negative, then the species is diffusing toward the GB.

At 10^{-7} dpa, the Cr flux through preferential coupling with vacancies is large and positive, suggesting the Cr atoms diffuse away from the GB, leading to depletion of Cr at GBs. On the other hand, the flux of Fe and Ni through vacancies is negative, suggesting they diffuse toward the GB, leading to enrichment of Fe and Ni at GBs. At the same time, the flux of Cr through the preferential coupling with interstitials is negative, leading to enrichment of Cr at the GB; and the fluxes of Fe and Ni through interstitials are positive, leading to depletion of Fe and Ni at GBs. The fluxes due to preferential coupling with interstitials are in opposite directions from those due to preferential coupling with vacancy. However, because of the much larger magnitudes of fluxes through vacancies than those through interstitials, the net fluxes of atoms are dominated

by those through vacancies. The results suggest the diffusion of all elements at this time is mainly via the vacancy mechanism.

At 10^{-5} dpa, the fluxes through vacancies maintain the same direction as those at 10^{-7} dpa with a slightly increased magnitude. However, the magnitude of the fluxes through interstitials is greatly enhanced at this step. Particularly, the Ni flux through interstitials is greater than the Ni flux through vacancies and becomes the dominant force for Ni diffusion, leading to the positive net flux of Ni. Although the diffusion fluxes of Cr and Fe through vacancies are still greater than those through interstitials, the magnitudes of their net fluxes are much smaller, near 1 order of magnitude smaller. At this step, the Cr (Fe) will continue depleting (enriching) but at a slower rate. The Ni will become depleting due to the net flux diffusing away from the GB. The dominant diffusion mechanism for Ni is interstitial diffusion.

At 10^{-3} dpa, the fluxes of Cr, Fe, and Ni are generally about the same as those at 10^{-5} dpa, except for those in the vicinity of GBs (<5 nm). In the vicinity of GBs (<5 nm), dramatic changes were observed in the fluxes through vacancies, but not in those through interstitials. This is caused by a composition gradient induced by segregation. The composition gradient in the vicinity of GBs imposes a chemical driving force for diffusion. This driving force is in an opposite direction from the driving force from the defect concentration gradient from bulk to sink. Therefore, the fluxes due to composition gradients at the GB counter the net fluxes through defects. As a result, the net flux of Cr, which originally increases monotonically with decreasing distance from the GB, now decreases in the vicinity of the GB, leading to a slower depletion rate. Similarly, the Fe will enrich at the GB at a slower rate. The fluxes of Cr and Fe due to the composition gradient are opposite to those through vacancies, i.e., the dominant fluxes. Unlike the case for Cr and Fe, the segregation of Ni is dominated by the interstitial flux, which causes the depletion of Ni at GBs. Therefore, the composition gradient of Ni drives a diffusion to send more Ni atoms to GBs and to reduce the depletion. At the same time, the Ni flux through vacancies also influences more Ni atoms to stay at GBs. Therefore, for Ni, the driving force due to the composition gradient has the same direction as those for diffusion through vacancies. Although the interstitial flux of Ni is more prevalent at distances further away from GBs, the combined flux due to vacancies and to the composition gradient is more prevalent in the vicinity of GBs. Therefore, Ni will be enriched again at GBs.

It should be explained why the composition dependence of flux through vacancies is more sensitive than that of interstitial flux. The composition dependence of the diffusion coefficient through vacancies is incorporated into the exponential term of the mobility models, but it is linear for diffusion through the interstitial binding model. Therefore, the fluxes through vacancies are more sensitive to composition variations. Figure 5 (a) shows the partial diffusion coefficient of Cr vs. the distance from GBs at different doses. It clearly shows these diffusion coefficients over different doses are kept constant at distances far away from the GB, but are significantly modified by the changing composition in the region close to the GB. Particularly, the composition dependence of DCrV is greater than that of DCrI at high dose levels where larger elemental segregation presents. This finding is consistent with Wolfer's work [29] in which he suggested that although the average diffusivity of alloy constituents through defects is hardly affected by segregation, the diffusion at GBs can be modified considerably. He also

suggested such modification is more significant to atomic fluxes through vacancies than those through interstitials.

At 10^{-1} dpa, the segregation or the composition gradient is extended to a broader distance away from GBs. Therefore, the diffusion fluxes through vacancies and interstitials are affected by the composition gradient over a broader distance from GBs. Furthermore, the magnitude of the segregation is larger than that at 10^{-3} dpa; therefore, the effect of composition gradient on the interstitial fluxes is visible. The magnitudes of the net fluxes are smaller than those at previous doses because of competition from the diffusion fluxes from different driving forces. At 10 dpa, the fluxes through vacancies and interstitials are of almost the same magnitude but are in opposite directions. The net fluxes of all three elements are close to zero, suggesting no further enrichment or depletion. Therefore, the system has reached a steady state at this dose.

4.3 Diffusion Mechanism

The evolution of the flux can shed light on the diffusion mechanism in concentrated Fe-Cr-Ni alloys if the relative magnitude of the flux through vacancies and interstitials is compared. As the magnitude of the diffusion flux is determined by the product of the partial diffusion coefficient and the defect concentration gradient, it is worthwhile to look into these two quantities as well. The partial diffusion coefficient and defect concentration are plotted in Fig. 5 (a) and (b). Only the results for Cr are presented here, but a similar analysis can be applied to Fe and Ni. At 10^{-7} dpa, the partial diffusion coefficient of Cr through vacancies at 10^{-7} dpa is more than one order of magnitude higher than that through interstitials, whereas the vacancy concentration gradient from bulk to GBs is not too different from its interstitial counterpart. Therefore, the magnitude of the diffusion flux through vacancies is dominant at this time, owing to the much larger partial diffusion coefficient via vacancies. Consequently, the net fluxes of Fe, Cr, and Ni are dominated by the fluxes through vacancies, and the major diffusion mechanism is via vacancies at this level. At 10^{-5} dpa, the magnitude of interstitial fluxes is greatly increased, while the magnitude of fluxes through vacancies is only slightly increased. This is because the concentration gradient of interstitials quickly increases by more than one order of magnitude over this period, but the gradient for vacancies does not. The reason is that the larger partial diffusion coefficient DCrV leads to higher sink defect capture rates of vacancies at dislocations. With increasing damage dose, more vacancies are lost at dislocations and more interstitials accumulate in the material, as shown in Fig. 5(b). Since the defect concentration at the random high-angle GB is fixed at the thermal equilibrium, i.e., a perfect sink boundary condition, the interstitial concentration gradient becomes larger than that of the vacancies. The quick increase in interstitial concentration gradient leads to increased diffusion fluxes to the GB through interstitials. The simulation results suggest that for Cr and Ni, the dominant diffusion mechanism is via vacancies; but for Ni, the diffusion swings from the vacancy-dominant mechanism at 10^{-7} dpa to the interstitial-dominant one at 10^{-5} dpa.

It could be argued that the magnitude of the interstitial diffusion flux is underestimated because the currently used effective migration energy (0.9 eV) for interstitials is too large or the jumping frequency (1.5×10^{12} s^{-1}) is too small. Therefore, a smaller migration energy of 0.2 eV and a larger jumping frequency of 1.5×10^{13} s^{-1} were also used to calculate the diffusion fluxes. The results show the magnitudes of interstitial fluxes of Cr and Fe are still far less than fluxes of

Cr and Fe through vacancies, but Ni interstitial flux at 10^{-7} dpa is now larger than that through vacancies This suggestes that the diffusion mechanism of Ni is interstitial-dominant. Therefore, the dramatic change in interstitial diffusion parameters would affect the diffusion mechanism of Ni but not that of Cr and Fe.

Which diffusion mechanism is dominant seems applicable only at low dpa. With increased dose, the flux via vacancies will be balanced by that via interstitials, and vice versa, as shown in Fig. 4.

4.4 Oscillatory behavior in RIS profile

The RIS profile obtained from experimental data does not always show a monotonic increase or decrease from bulk to GBs. This phenomenon is particularly prominent for the Fe segregation profile in Fig. 1, in which the Fe concentration from bulk to GB initially increases, and then decreases in the vicinity of GBs (<2.5 nm). This phenomenon is due to the competition of two driving forces. At the initial time of irradiation, the system is mainly subjected to one driving force, which is the concentration gradient of defects from bulk to sink (GB). After a prolonged time, the concentration gradient of elemental species at GBs is built up as a result of segregation. Such a built-up gradient is largest at the region of the GB (<2.5 nm) and imposes a chemical force that counters the diffusion flux due to the defect gradient.

The competition between these two driving forces not only leads to the non-monotonic shape of the RIS profile as a function of distance from GBs, but also accounts for a possible flip of elemental segregation as a function of dose. Table 3 lists the net fluxes of Cr, Fe, and Ni at the first 10 nodes from the GB at different dose levels. The positive flux values are listed in shaded boxes; the box without shading is for negative fluxes. When there is a change from the shaded to the unshaded box, or vice versa, a flip of elemental segregation occurs. The table shows the negative fluxes for Fe from 10^{-7} to 10^{-3} dpa, suggesting enrichment of Fe during this period, because a negative sign means the atoms flow toward the GB. It also shows that the magnitude of the fluxes decreases with increasing dose, suggesting the increasing role of diffusion driven by segregation itself at the GB. At 10^{-1} dpa, the fluxes very close to the GB become positive, whereas those in regions farther away from the GB remain negative. At this time, depletion of Fe occurs at the GB, although enrichment of Fe in the region farther from GB still exists. Therefore, the segregation of Fe at the GB is flipped from enrichment to depletion. By close examination of the fluxes of Ni, two flips were predicted. The first flip was from enrichment to depletion at a dose between 10^{-7} and 10^{-5} dpa. The underlying reason for this flip is that Ni diffusion was changing from vacancy-dominant to interstitial-dominant diffusion. The second flip was from depletion to enrichment. This flip was due to the additional flux driven by the elemental composition gradient at the GB. The fluxes driven by both the vacancy concentration gradient and the composition gradient of Ni influence more Ni to stay at the GB, leading to a second enrichment. The flip from enrichment to depletion of elements, or vice versa, can also be demonstrated by plotting the net diffusion flux of elements in Fig. 6. The Cr, Fe, Ni composition profile at 10^{-7} and 0.1dpa are shown in Fig. 7, denoted by dash and solid lines, respectively. At 10^{-7}, negligible composition gradient is formed at GB. But at 0.1 dpa, w-shape profiles of Cr, Fe and Ni were formed due to combined effect of local composition gradient and preferential coupling between atoms and defects.

In summary, the oscillatory behavior of alloy compositions at GB is a result of multiple factors, such as vacancy gradient, interstitial gradient, unequal mobility of alloy constituents and their compositional dependence, and the composition gradient induced by the segregation itself.

Table 3 The net fluxes of Cr, Fe, and Ni at the first 10 nodes from GB at different dose levels

Distance from GB(nm)	10^{-7}dpa	10^{-5} dpa	10^{-3} dpa	10^{-1} dpa	10 dpa
Cr					
0	4.24E+14	2.71E+14	1.08E+14	2.81E+11	5.19E+09
0.19706	4.23E+14	2.73E+14	2.01E+14	1.26E+12	6.17E+09
0.40966	4.22E+14	2.72E+14	2.39E+14	2.52E+12	3.35E+09
0.63902	4.21E+14	2.71E+14	2.54E+14	4.02E+12	4.32E+09
0.88645	4.20E+14	2.70E+14	2.59E+14	5.74E+12	7.14E+09
1.15339	4.18E+14	2.69E+14	2.60E+14	7.70E+12	7.48E+09
1.44137	4.17E+14	2.68E+14	2.60E+14	9.88E+12	7.96E+09
1.75205	4.16E+14	2.66E+14	2.59E+14	1.23E+13	9.87E+09
2.08722	4.14E+14	2.65E+14	2.57E+14	1.50E+13	1.18E+10
2.44881	4.12E+14	2.63E+14	2.56E+14	1.79E+13	1.36E+10
Fe					
0	−3.69E+14	−2.93E+14	−1.04E+14	1.13E+12	6.91E+08
0.19706	−3.68E+14	−2.96E+14	−2.14E+14	1.89E+12	1.77E+09
0.40966	−3.67E+14	−2.95E+14	−2.61E+14	2.07E+12	1.88E+09
0.63902	−3.66E+14	−2.94E+14	−2.78E+14	1.82E+12	4.94E+09
0.88645	−3.64E+14	−2.93E+14	−2.84E+14	1.19E+12	7.96E+09
1.15339	−3.63E+14	−2.92E+14	−2.85E+14	2.06E+11	8.50E+09
1.44137	−3.62E+14	−2.90E+14	−2.85E+14	−1.14E+12	9.68E+09
1.75205	−3.60E+14	−2.89E+14	−2.83E+14	−2.84E+12	1.14E+10
2.08722	−3.58E+14	−2.87E+14	−2.82E+14	−4.91E+12	1.25E+10
2.44881	−3.57E+14	−2.85E+14	−2.80E+14	−7.35E+12	1.34E+10
Ni					
0	−5.50E+13	2.26E+13	-4.25E+12	−1.41E+12	−5.88E+09
0.19706	−5.51E+13	2.30E+13	1.36E+13	−3.14E+12	−7.95E+09
0.40966	−5.52E+13	2.30E+13	2.14E+13	−4.59E+12	−5.21E+09
0.63902	−5.52E+13	2.29E+13	2.40E+13	−5.84E+12	−9.26E+09
0.88645	−5.53E+13	2.28E+13	2.48E+13	−6.94E+12	−1.51E+10
1.15339	−5.54E+13	2.26E+13	2.49E+13	−7.90E+12	−1.60E+10
1.44137	−5.55E+13	2.25E+13	2.48E+13	−8.75E+12	−1.76E+10
1.75205	−5.56E+13	2.24E+13	2.47E+13	−9.47E+12	−2.13E+10
2.08722	−5.57E+13	2.22E+13	2.46E+13	−1.01E+13	−2.43E+10
2.44881	−5.58E+13	2.21E+13	2.44E+13	−1.05E+13	−2.70E+10

5. Conclusions

This work presented a detailed analysis of the diffusion fluxes induced by preferential atom-vacancy and atom-interstitial coupling under simultaneous thermal and irradiation conditions. The diffusion flux equations were based on the Perks model formulated through the linear theory of TIP. Both the cross and non-cross phenomenological diffusion coefficients in the flux equations were considered and correlated with tracer diffusion coefficients through Manning's relations. Preferential atom-vacancy coupling was described by the mobility model and preferential atom-interstitial coupling by the interstitial binding model. The composition dependence of the thermodynamic factor was modeled using the CALPHAD approach.

The diffusion fluxes at 10^{-7}, 10^{-5}, 10^{-3}, 10^{-1} and 10 dpa were calculated and analyzed in terms of contributions from preferential atom-vacancy coupling, atom-interstitial coupling, and composition gradient induced by segregation. The following conclusions can be drawn from this work:

1. The dominant diffusion mechanism for Cr and Fe is via vacancies, whereas that for Ni can swing from a vacancy-dominant to a interstitial-dominant mechanism. The current modeling suggests that the interstitial diffusion mechanism for Ni in Fe-Cr-Ni austenitic alloys is highly competitive with the vacancy mechanism. For all elements, which diffusion mechanism is dominant seems applicable only at the initial time of irradiation. With increasing dose, the magnitudes of the diffusion fluxes from all sources change dynamically until they reach a balance.
2. The diffusion flux in the vicinity of the GB was found to be greatly modified by the segregation induced by irradiation, leading to a nonmonotonic w-shape of RIS profiles at steady state. It also leads to a flip of elemental enrichment or depletion before the system reaches the steady state.

This work establishes that both vacancy and interstitial diffusion, and segregation itself, all have important roles in determining the microchemistry of Fe, Cr, and Ni at GBs.

6. References

1. Nolfi, F.V., Jr. and Editor, *Phase Transformations During Irradiation*. 1983: Applied Science Publishers. 363 pp.

2. Russell, K.C., *Phase stability under irradiation.* Prog. Mater. Sci., 1984. **28**(3-4): p. 229–434.

3. Was, G., *Fundamentals of Radiation Materials Science*. 2007, Berlin: Springer-Verlag.

4. Wiedersich, H. and P.R. Okamoto. *Effects of radiation-induced segregation on phase stability*. 1981. Metall. Soc. AIME.

5. Zinkle, S. and J. Busby, *Structural materials for fission and fusion energy.* Materials Today, 2009. **12**: p. 12–19.

6. Nastar, M. and F. Soisson. *Radiation-induced segregation*. 2012. Elsevier B.V.

7. Allen, T., et al., *On the mechanism of radiation-induced segregation in austenitic Fe–Cr–Ni alloys.* Journal of Nuclear Materials, 1998. **255**(1): p. 44–58.

8. Allen, T., G. Was, and E. Kenik, *The effect of alloy composition on radiation-induced segregation in Fe-Cr-Ni alloys.* Journal of Nuclear Materials, 1997. **244**(3): p. 278–294.

9. Takahashi, H. and N. Hashimoto, *Radiation-induced segregation and grain boundary migration in Fe–Cr–Ni model alloy under irradiation.* Materials Transactions, JIM, 1993. **34**(11): p. 1027–1030.

10. Watanabe, S., et al., *Quantitative studies of irradiation-induced segregation and grain boundary migration in Fe Cr Ni alloy.* Journal of Nuclear Materials, 1995. **224**(2): p. 158–168.

11. Busby, J., et al. *Influence of initial grain boundary composition on the evolution of radiation-induced segregation profiles*. in *MRS Proceedings*. 1998. Cambridge Univ Press.

12. Kenik, E., et al. *Origin and influence of pre-existing segregation on radiation-induced segregation in austenitic stainless steels*. in *MRS Proceedings*. 1998. Cambridge Univ Press.

13. Damcott, D., T. Allen, and G. Was, *Dependence of radiation-induced segregation on dose, temperature and alloy composition in austenitic alloys.* Journal of Nuclear Materials, 1995. **225**: p. 97–107.

14. Lam, N., *Compositional changes in Fe-Cr-Ni alloys under proton bombardment at elevated temperatures.* Journal of Nuclear Materials, 1983. **117**: p. 106–112.

15. Okamoto, P. and L. Rehn, *Radiation-induced segregation in binary and ternary alloys.* Journal of Nuclear Materials, 1979. **83**(1): p. 2–23.

16. Marwick, A., *Segregation in irradiated alloys: the inverse Kirkendall effect and the effect of constitution on void swelling.* Journal of Physics F: Metal Physics, 1978. **8**(9): p. 1849.

17. Smigelskas, A. and E. Kirkendall, *Zinc diffusion in alpha brass.* Trans. Aime, 1947. **171**: p. 130–142.

18. Perks, J.M., A.D. Marwick, and C.A. English, *AERE R.* 1986. p. 12121.

19. Allen, T.R. and G.S. Was, *Modeling of radiation-induced segregation in austenitic Fe-Cr-Ni alloys.* Mater. Res. Soc. Symp. Proc., 1997. **439** (Microstructure Evolution during Irradiation): p. 539–544.

20. Wiedersich, H., P.R. Okamoto, and N.Q. Lam, *A theory of radiation-induced segregation in concentrated alloys.* J. Nucl. Mater., 1979. **83**(1): p. 98–108.

21. Murphy, S., *Contribution of interstitial migration to segregation in concentrated alloys.* Journal of Nuclear Materials, 1991. **182**: p. 73–86.

22. Hashimoto, T., Y. Isobe, and N. Shigenaka, *A model for radiation-induced segregation in fcc binary alloys.* Journal of Nuclear Materials, 1995. **225**: p. 108–116.

23. Jönsson, B., *Assessment of the mobility of carbon in fcc C-Cr-Fe-Ni alloys.* Zeitschrift für Metallkunde, 1994. **85**(7): p. 502–509.

24. Kaufman, L., et al., *Coupled pair potential, thermochemical and phase diagram data for transition metal binary systems. VII.* CALPHAD: Comput. Coupling Phase Diagrams Thermochem., 1984. **8**(1): p. 25–66.

25. Lukas, H.L., S.G. Fries, and B. Sundman, *Computational thermodynamics: the CALPHAD method*. Vol. 131. 2007: Cambridge University Press, Cambridge.

26. Saunders, N. and A.P. Miodownik, *CALPHAD (Calculation of Phase Diagrams): A Comprehensive Guide: A Comprehensive Guide*. Vol. 1. 1998: Elsevier.

27. Klaver, T., D. Hepburn, and G. Ackland, *Defect and solute properties in dilute Fe-Cr-Ni austenitic alloys from first principles.* Physical Review B, 2012. **85**(17): p. 174111.

28. Field, K.G., et al., *Defect sink characteristics of specific grain boundary types in 304 stainless steels under high dose neutron environments.* Acta Materialia, 2015. **89**: p. 438–449.

29. Wolfer, W.G., *Drift forces on vacancies and interstitials in alloys with radiation-induced segregation.* J. Nucl. Mater., 1983. **114**(2-3): p. 292–304.

30. Manning, J.R., *Correlation factors for diffusion in nondilute alloys.* Phys. Rev. B, 1971. **[3]4**(4): p. 1111–21.

31. Lidiard, A.B., *A note on Manning's relations for concentrated multicomponent alloys.* Acta Metall., 1986. **34**(8): p. 1487–90.

32. Belova, I. and G. Murch, *A new analysis of diffusion in ternary alloys: application to FCC Fe-Ni-Cr alloys.* Acta Materialia, 2002. **50**(18): p. 4617–4627.

33. Belova, I., et al., *Theoretical analysis of experimental tracer and interdiffusion data in Cu–Ni–Fe alloys.* Acta Materialia, 2005. **53**(17): p. 4613–4622.

34. Redlich, O. and A. Kister, *Algebraic representation of thermodynamic properties and the classification of solutions.* Industrial & Engineering Chemistry, 1948. **40**(2): p. 345–348.

35. Janssens, K., et al., *Computational Materials Engineering, An Introduction to Microstructure Evolution*. 2007, USA: ELSEVIER.

36. Dinsdale, A.T., *SGTE data for pure elements.* CALPHAD: Comput. Coupling Phase Diagrams Thermochem., 1991. **15**(4): p. 317–425.

37. Muggianu, Y.M., M. Gambino, and J.P. Bros, *Enthalpies of formation of liquid alloys bismuth-gallium-tin at 723.deg.K. Choice of an analytical representation of integral and partial excess functions of mixing.* J. Chim. Phys. Phys.-Chim. Biol., 1975. **72**(1): p. 83–8.

38. Yang, Y. and J.T. Busby, *Thermodynamic modeling and kinetics simulation of precipitate phases in AISI 316 stainless steels.* J. Nucl. Mater., 2014. **448**(1-3): p. 282–293.

39. Rothman, S.J., L.J. Nowicki, and G.E. Murch, *Self-diffusion in austenitic iron-chromium-nickel alloys.* J. Phys. F, 1980. **10**(3): p. 383–98.

40. Million, B., J. Ruzickova, and J. Vrestal, *Diffusion in iron-nickel-chromium alloys with an fcc. lattice.* Mater. Sci. Eng., 1985. **72**(1): p. 85–100.

41. Ericsson, T., et al., *Some observations on interdiffusion in the Fe-Cr-Ni system.* J Iron Steel Inst., 1970. **208**(12): p. 1109–1110.

42. Hancock, G. and G. Leak, *Diffusion of nickel in binary alloys of iron with nickel, manganese, and chromium.* Metal Science, 1967. **1**(1): p. 33–36.

43. Kale, G., et al., *Ternary diffusion in FCC phase of Fe–Ni–Cr alloy system at 1223 K.* Materials Transactions, JIM, 1991. **32**(11): p. 1034–1041.

44. Cao, W., et al., *PANDAT software with PanEngine, PanOptimizer and PanPrecipitation for multi-component phase diagram calculation and materials property simulation.* CALPHAD, 2009. **33**(2): p. 328–342.

45. Guiraldenq, P. and P. Poyet, *Influence of nickel on the volume and intercrystalline diffusion in austenitic Fe-Cr-Ni alloys- Grain boundary energy evolution as a function of composition.* Memoires Scientifiques de la Revue de Metallurgie, 1973. **70**: p. 715–723.

46. Perkins, R.A., *Tracer diffusion of nickel-63 in iron-17 wt. pct. chromium-12 wt. pct. nickel.* Met. Trans., 1973. **4**(7): p. 1665–9.

47. Perkins, R.A., R.A. Padgett, and N.K. Tunali, *Tracer diffusion of iron-59 and chromium-51 in iron-17 wt. % chromium -12 wt. % nickel austenitic alloy.* Met. Trans., 1973. **4**(11): p. 2535–40.

48. Duh, J.G. and M.A. Dayananda. *Interdiffusion in Fe-Ni-Cr Alloys at 100° C.* in *Defect and Diffusion Forum*. 1991. Trans Tech Publ.

49. Edwards, D., A. Schemer-Kohrn, and S. Bruemmer, *Characterization of neutron-irradiated 300-series stainless steels.* EPRI, Palo Alto, CA, 2006. **1009896**.

50. Ehrhart, P., *Properties and interactions of atomic defects in metals and alloys, Landolt-Börnstein, New Series III, Vol. 25*. 1991, Springer, Berlin.

51. Barnard, L., et al., *Modeling radiation induced segregation in Ni–Cr model alloys from first principles.* Journal of Nuclear Materials, 2012. **425**(1–3): p. 8–15.

52. Delczeg, L., B. Johansson, and L. Vitos, *Ab initio description of monovacancies in paramagnetic austenitic Fe-Cr-Ni alloys.* Physical Review B, 2012. **85**(17): p. 174101.

53. Schön, C. and G. Inden, *Concentration dependence of the excess specific heat capacity and of the thermodynamic factor for diffusion in FCC and BCC ordering systems.* Acta Materialia, 1998. **46**(12): p. 4219–4231.

54. Karpe, N., et al., *The thermodynamic factor in interdiffusion: A strong effect in amorphous Ni-Zr.* Acta Metallurgica et Materialia, 1995. **43**(2): p. 551–558.

55. Fukuya, K., *Current understanding of radiation-induced degradation in light water reactor structural materials.* Journal of Nuclear Science and Technology, 2013. **50**(3): p. 213–254.

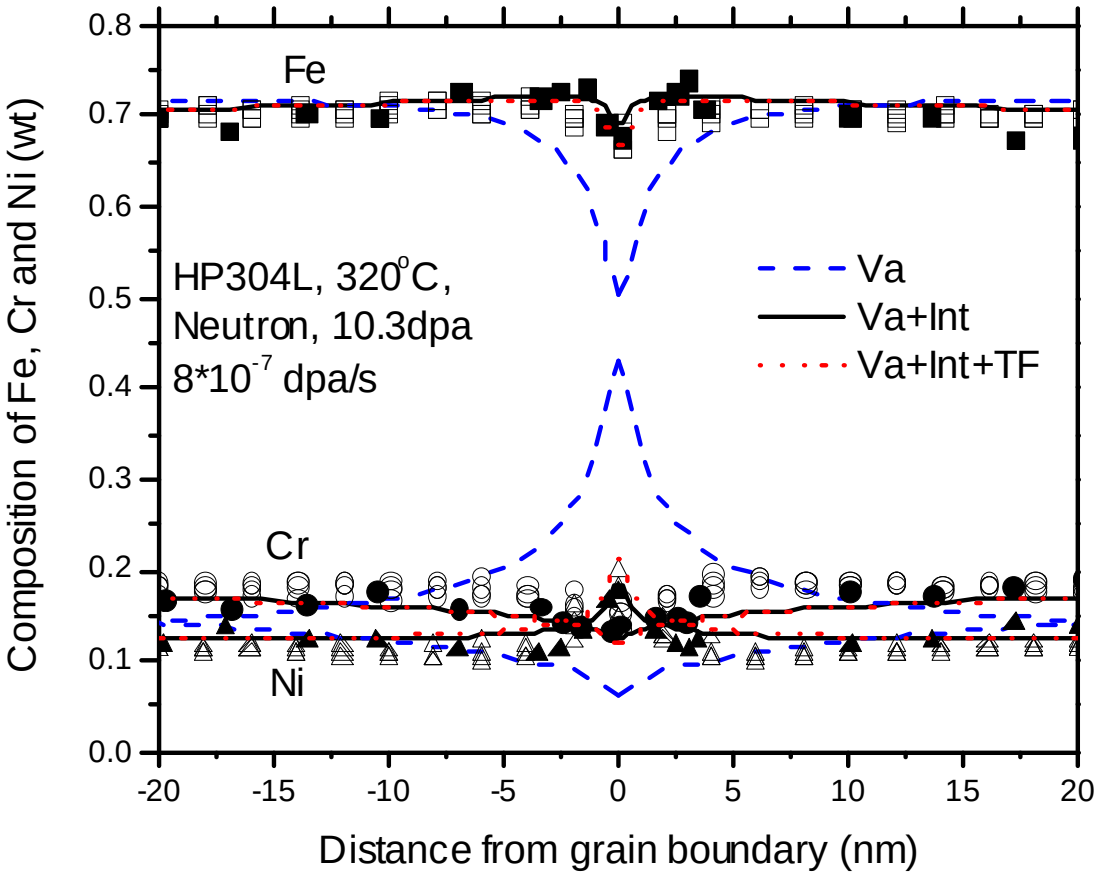

Figure 1 Comparison between the calculated RIS profile across the grain boundary and the experimental data [49]. Dashed line: preferential atom-vacancy coupling only and thermodynamic factor of "1"; solid line: both preferential atom-vacancy and atom-interstitial coupling and thermodynamic factor of "1"; dotted line: both preferential atom-vacancy and atom-interstitial coupling and thermodynamic factor as a function of composition. Open symbols represent data from Kevin and solid symbols represent Edwards' data.

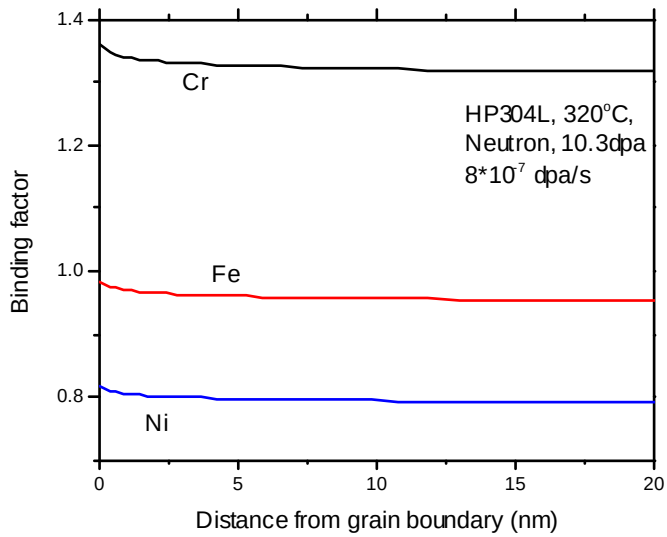

Figure 2 Calculated binding factors of Fe, Cr, and Ni as a function of distance from a high-angle random grain boundary

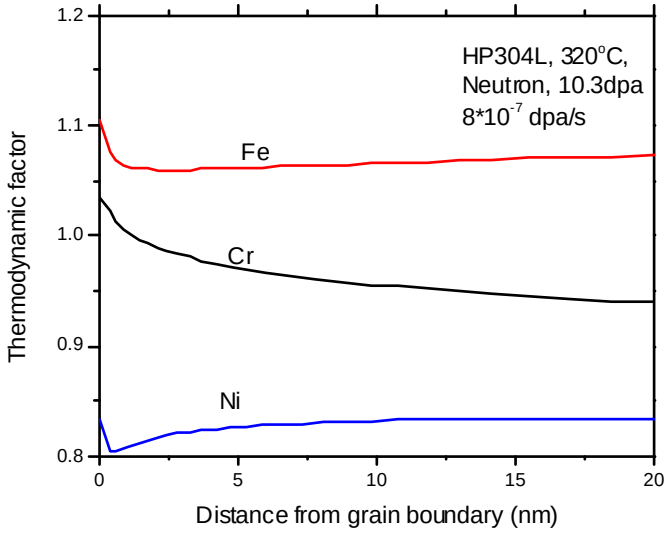

Figure 3 Calculated thermodynamic factors of Fe, Cr, and Ni as a function of distance from a high-angle random grain boundary.

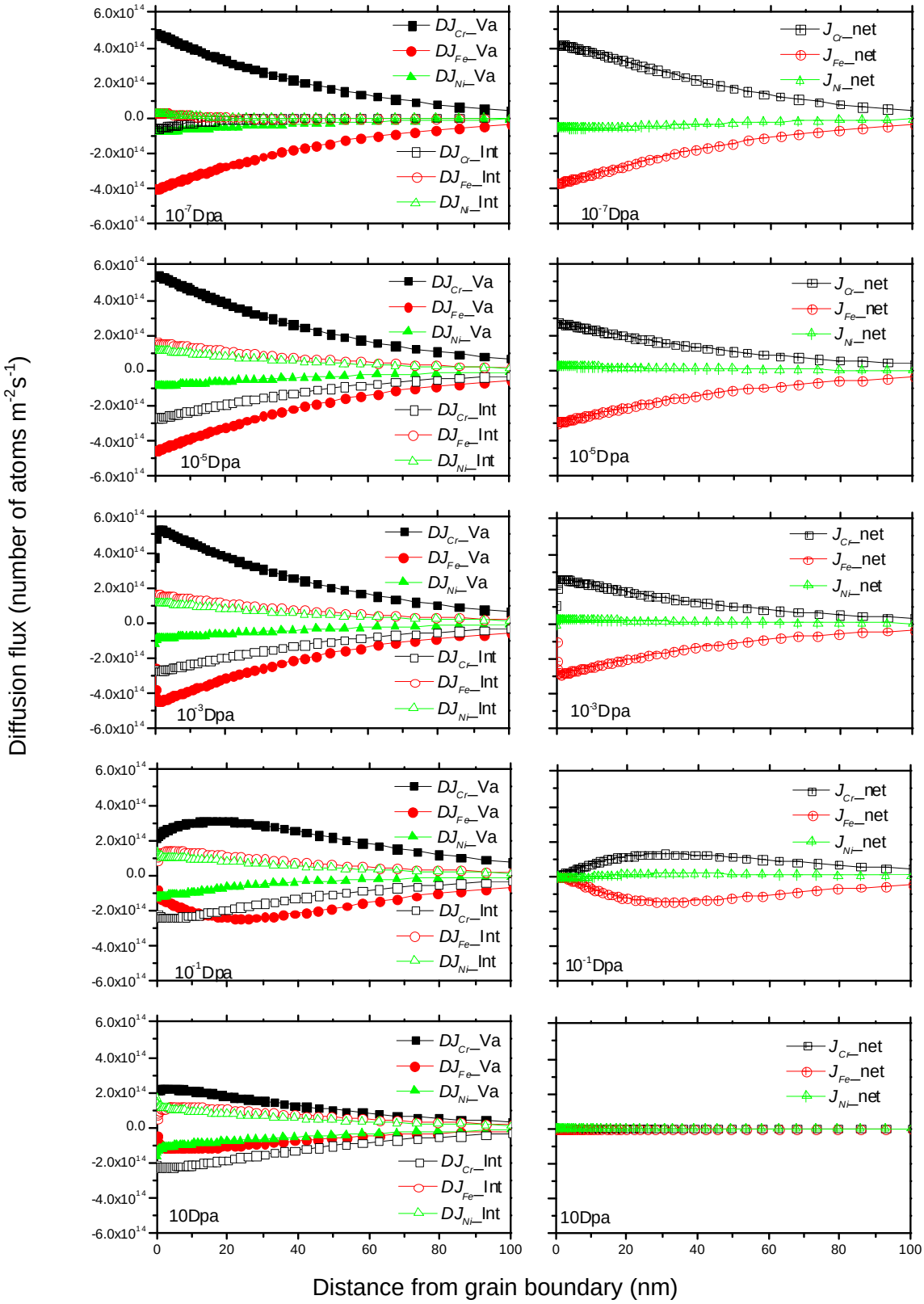
Diffusion flux (number of atoms m-2s-1)
Distance from grain boundary (nm)
DJCr_Va
DJFe_Va
DJNi_Va
DJCr_Int
DJFe_Int
DJNi_Int
JCr_net
JFe_net
JNi_net
10-7Dpa
10-5Dpa
10-3Dpa
10-1Dpa
10Dpa
6.0x10^14
4.0x10^14
2.0x10^14
0.0
-2.0x10^14
-4.0x10^14
-6.0x10^14
0
20
40
60
80
100

Figure 4 Calculated diffusion fluxes of Cr, Fe, and Ni as a function of distance from the grain boundary at different dose levels of 10^{-7}, 10^{-5}, 10^{-3}, 10^{-1} and 10 dpa. The square, circle, and triangle denote the Cr, Fe, and Ni fluxes, respectively. The solid symbol denotes flux through vacancies and the open symbol denotes flux through interstitials. The net flux is denoted by cross open symbols.

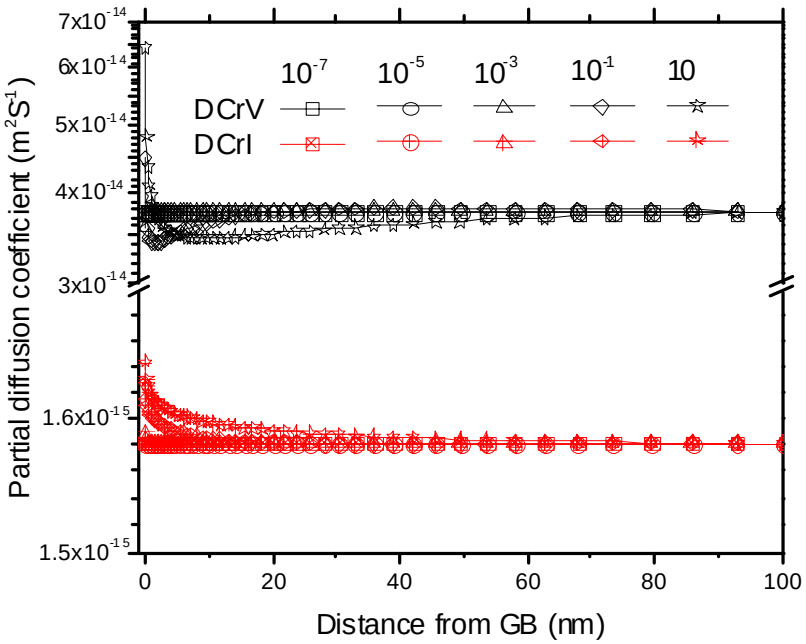

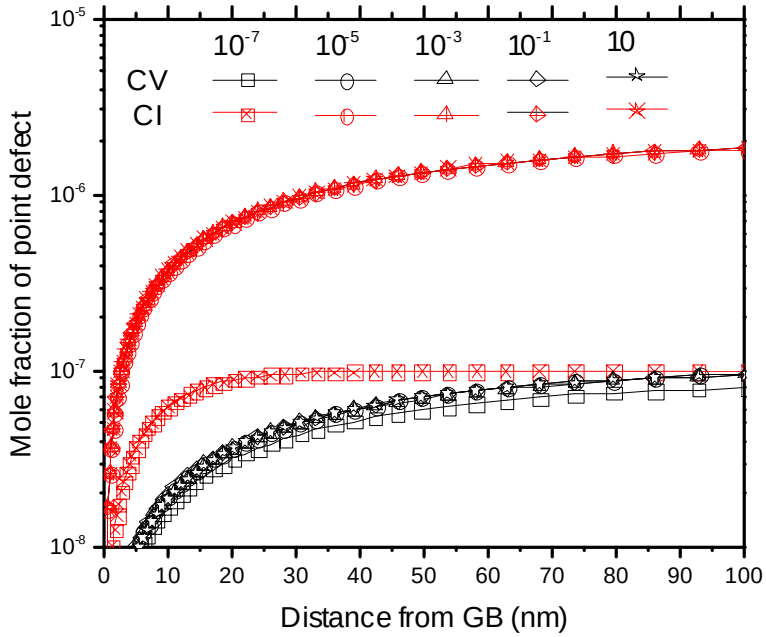

Figure 5 (a) Partial diffusion coefficient of chromium and (b) concentration of defects at 10^{-7}, 10^{-5}, 10^{-3}, 10^{-1} , 10 dpa.

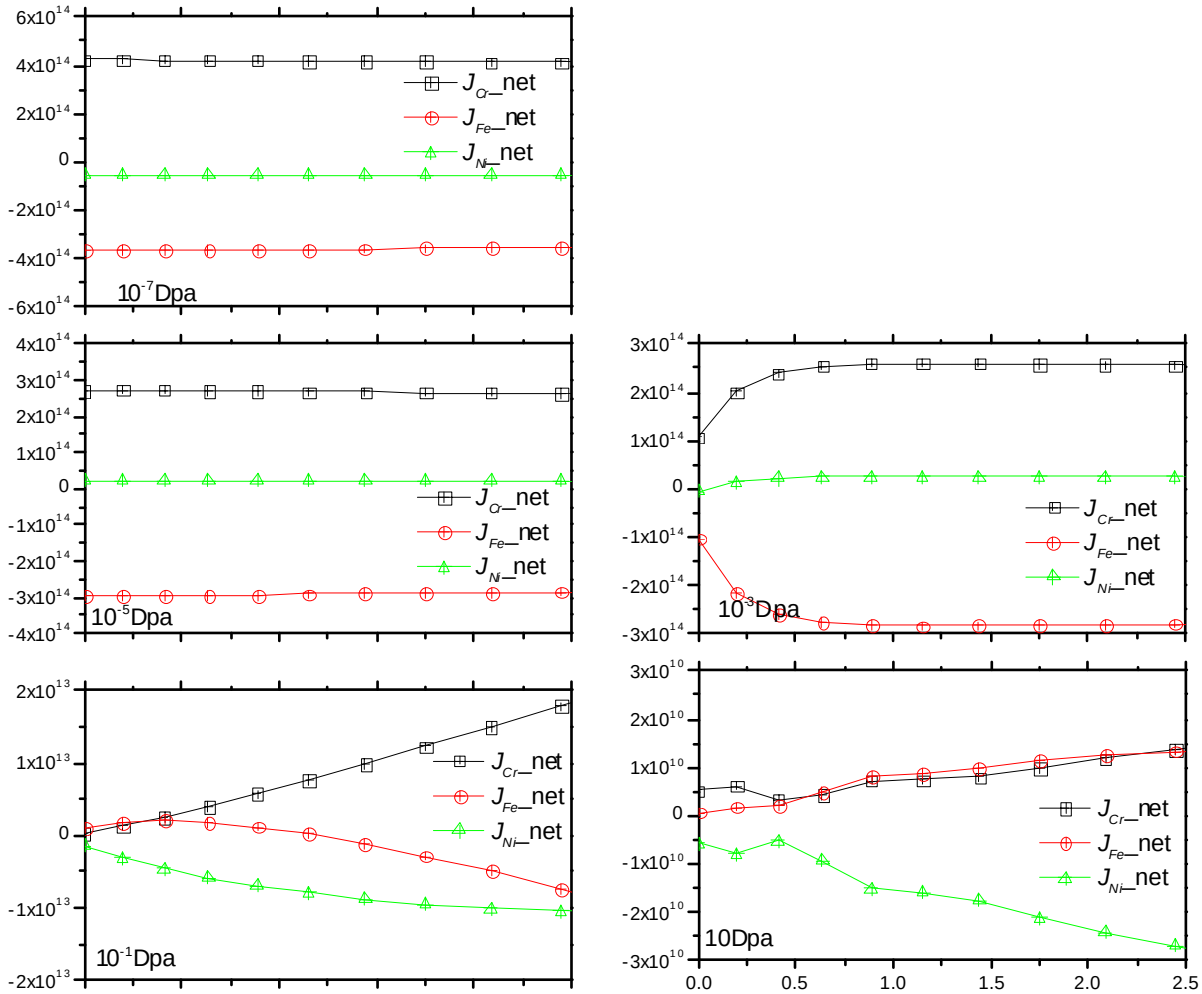

Figure 6 Calculated net diffusion flux of Fe, Cr and Ni showing flip of Fe from enrichment at 10^{-7}~10^{-3} dpa to depletion at 10^{-1}~10 dpa, and flip of Ni from enrichment at 10^{-7} dpa to depletion at 10^{-5} dpa and then from depletion at 10^{-5}~10^{-3} dpa to enrichment at 10^{-1}~10 dpa.

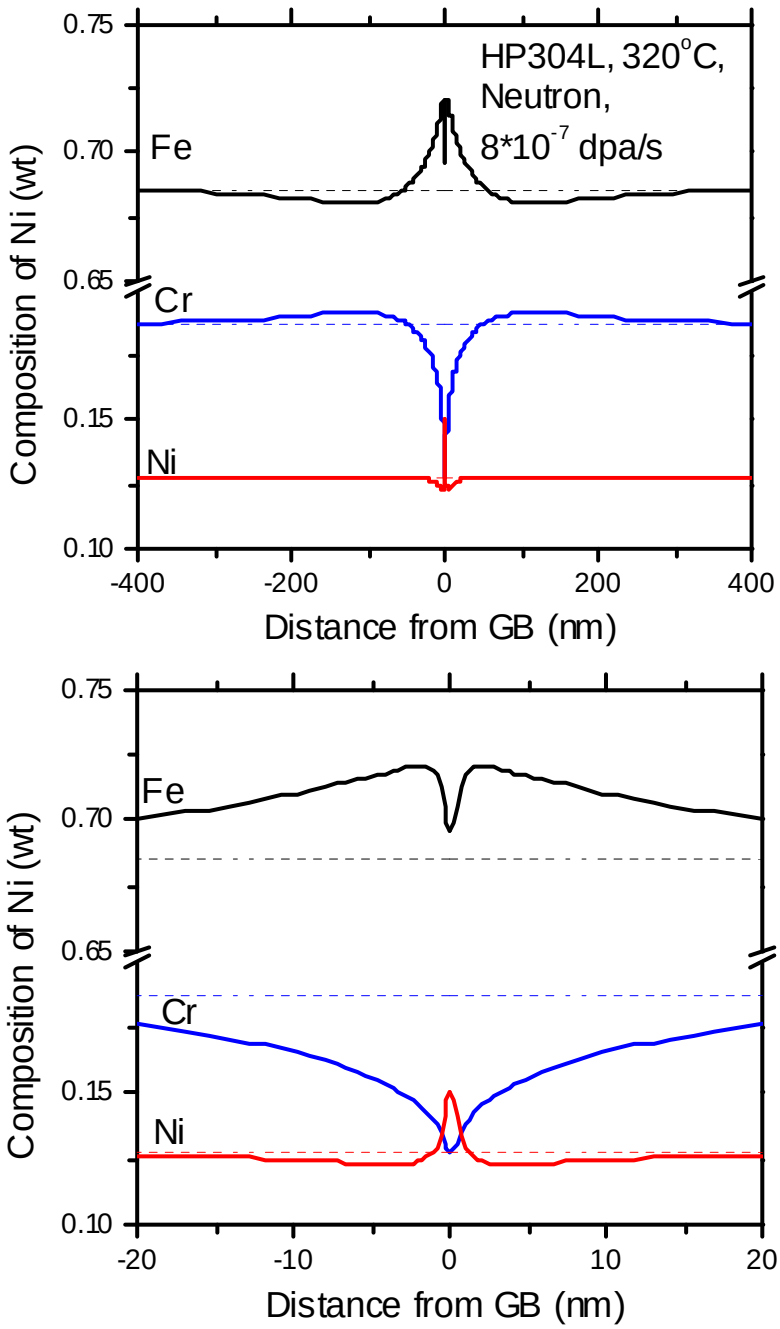

Figure 7 Calculated segregation profiles of Fe and Ni showing w-shape at 0.1 dpa (solid line) and 10^{-7} dpa (dash line). (a) full scale (b) enlarged region at GB.

7. Appendix

7.1 Comparison between the calculated tracer diffusion coefficient from the current mobility model and the experimental data

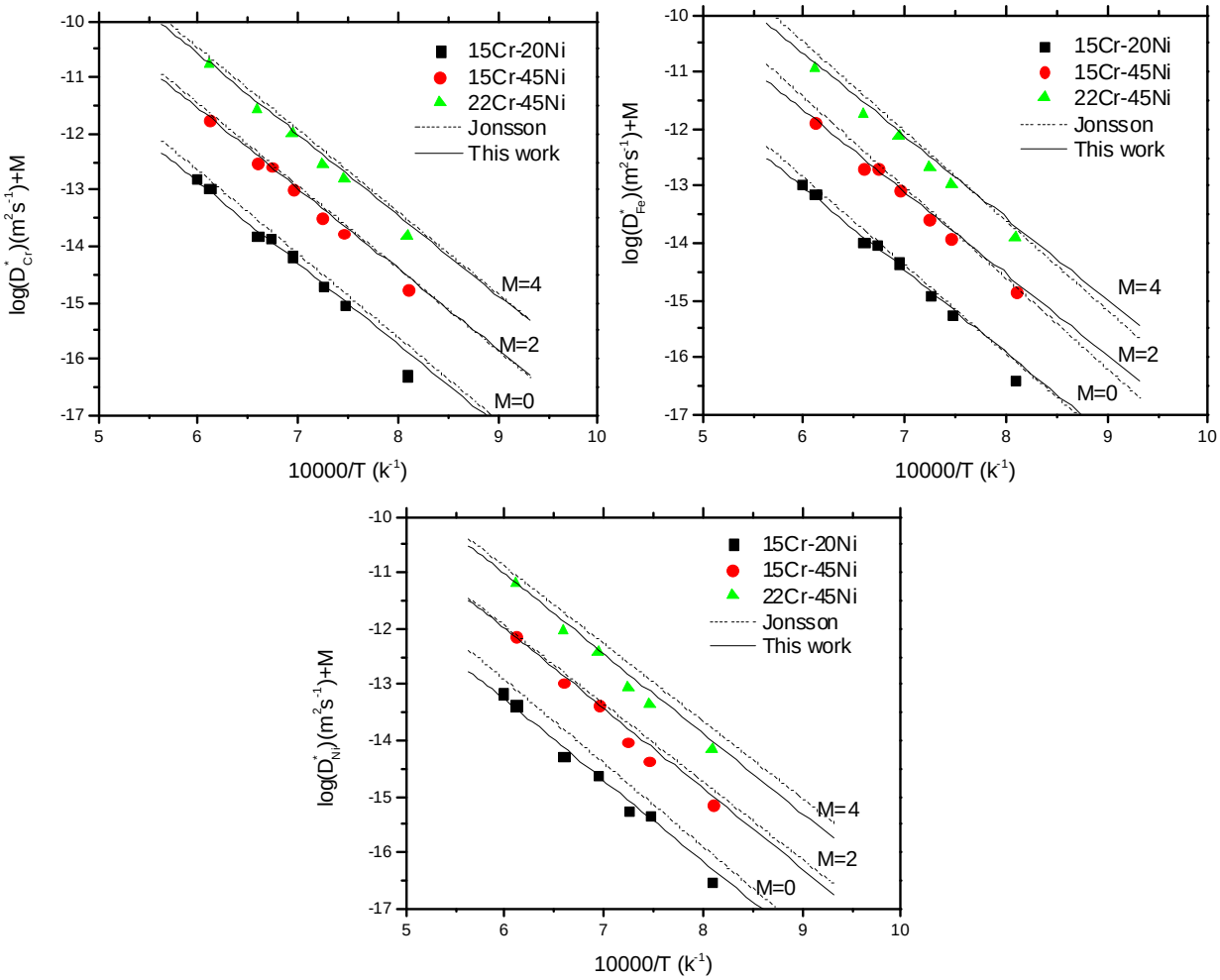

Figure 8 Comparison between the calculated tracer diffusion coefficient of Cr, Fe Ni (solid line: this work; dash line: Jönsson [23]) and experimental data from Rothman et al.[39].

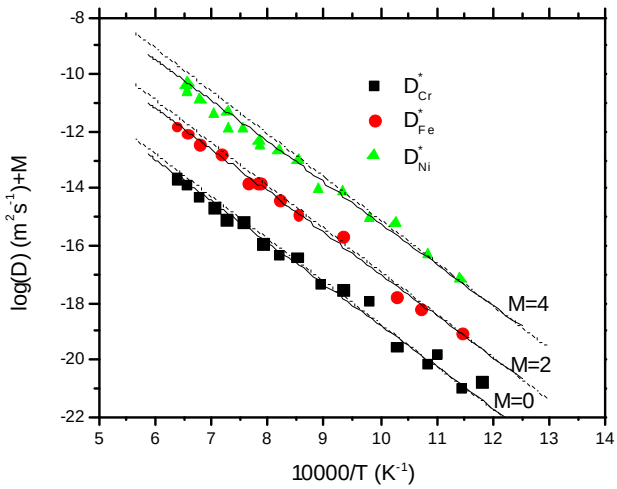

Figure 9 Comparison between the calculated tracer diffusion coefficient of Cr, Fe Ni (solid line: this work; dash line: Jönsson [23]) and experimental data from Perkins et al.[46-47]

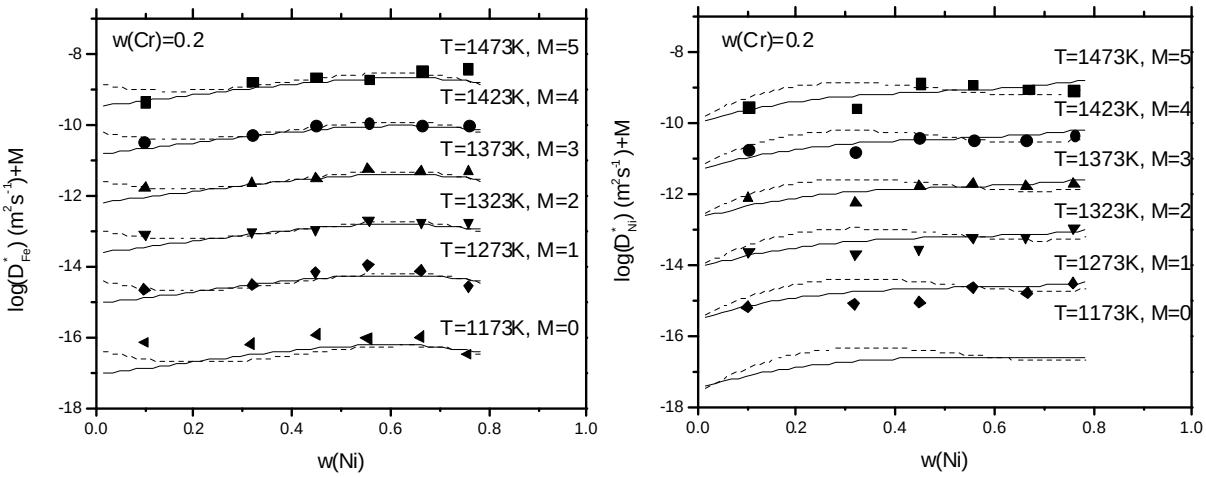

Figure 10 Comparison between the calculated tracer diffusion coefficient of Fe and Ni (solid line: this work; dash line: Jönsson [23]) and experimental data from Guiraldenq et al.[45].

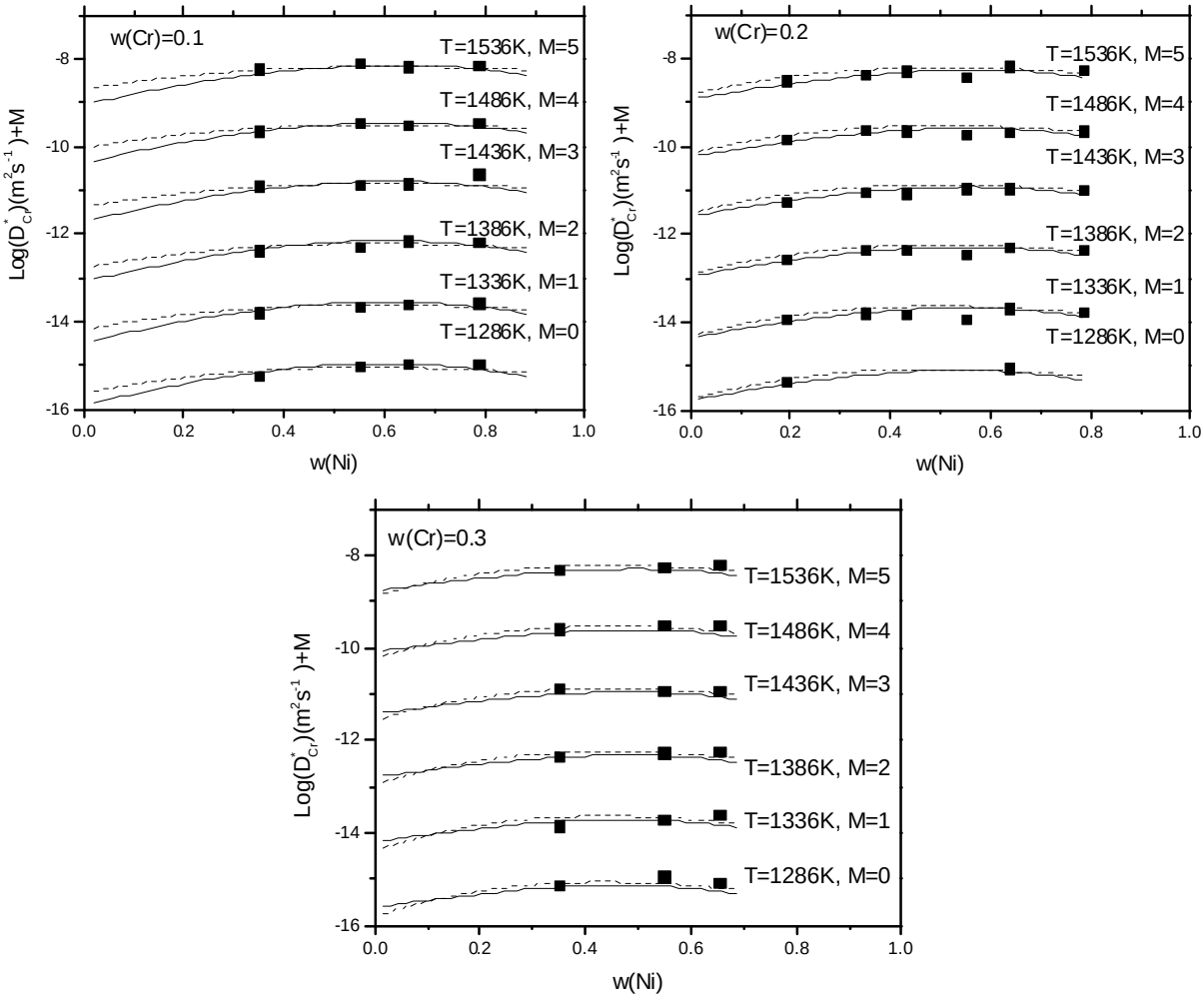

Figure 11 Comparison between the calculated tracer diffusion coefficient of Cr (solid line: this work; dash line: Jönsson [23]) and experimental data from Million et al.[40].

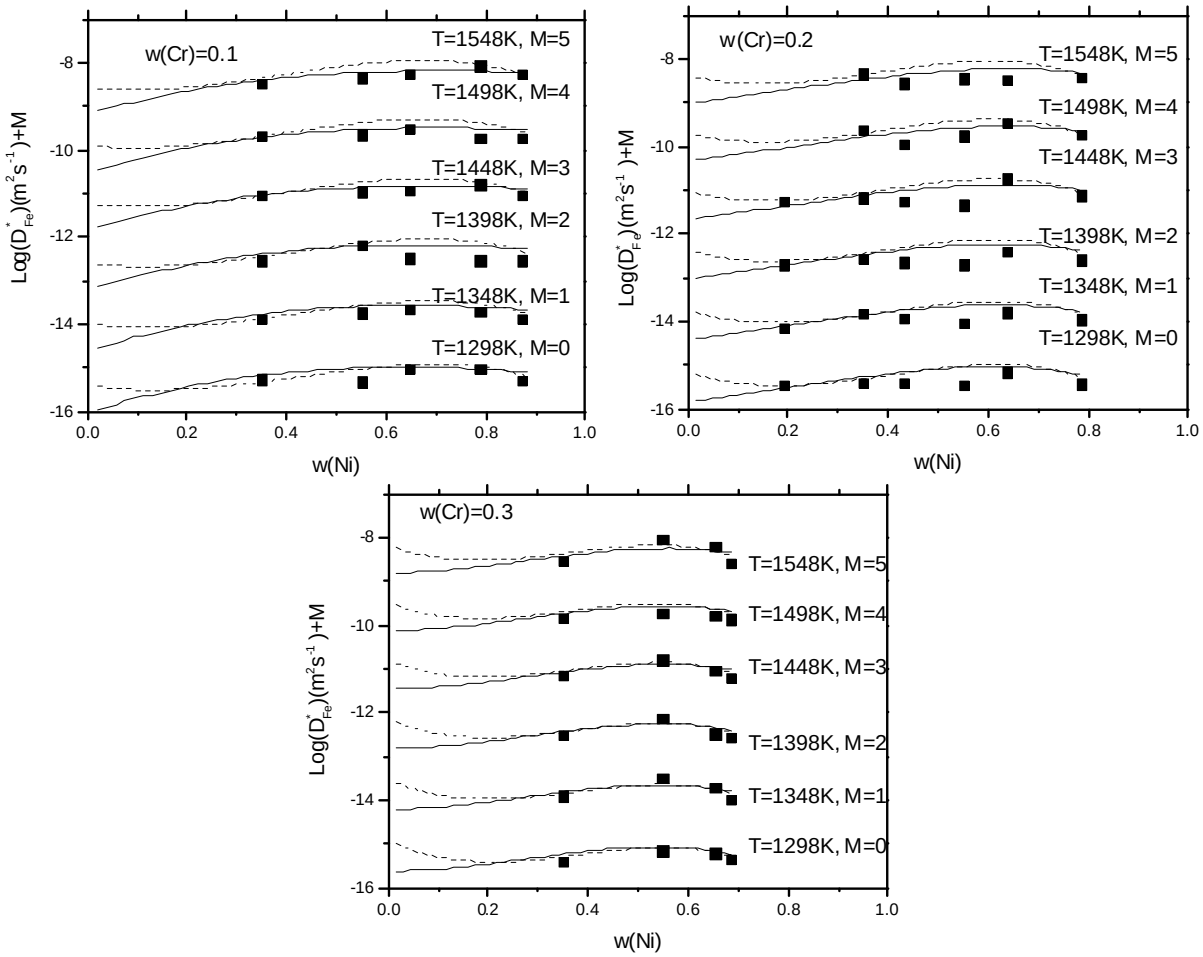

Figure 12 Comparison between the calculated tracer diffusion coefficient of Fe (solid line: this work; dash line: Jönsson [23]) and experimental data from Million et al.[40].

7.2 Validation of the current model parameters with experimental data [19] that were not used for optimization.

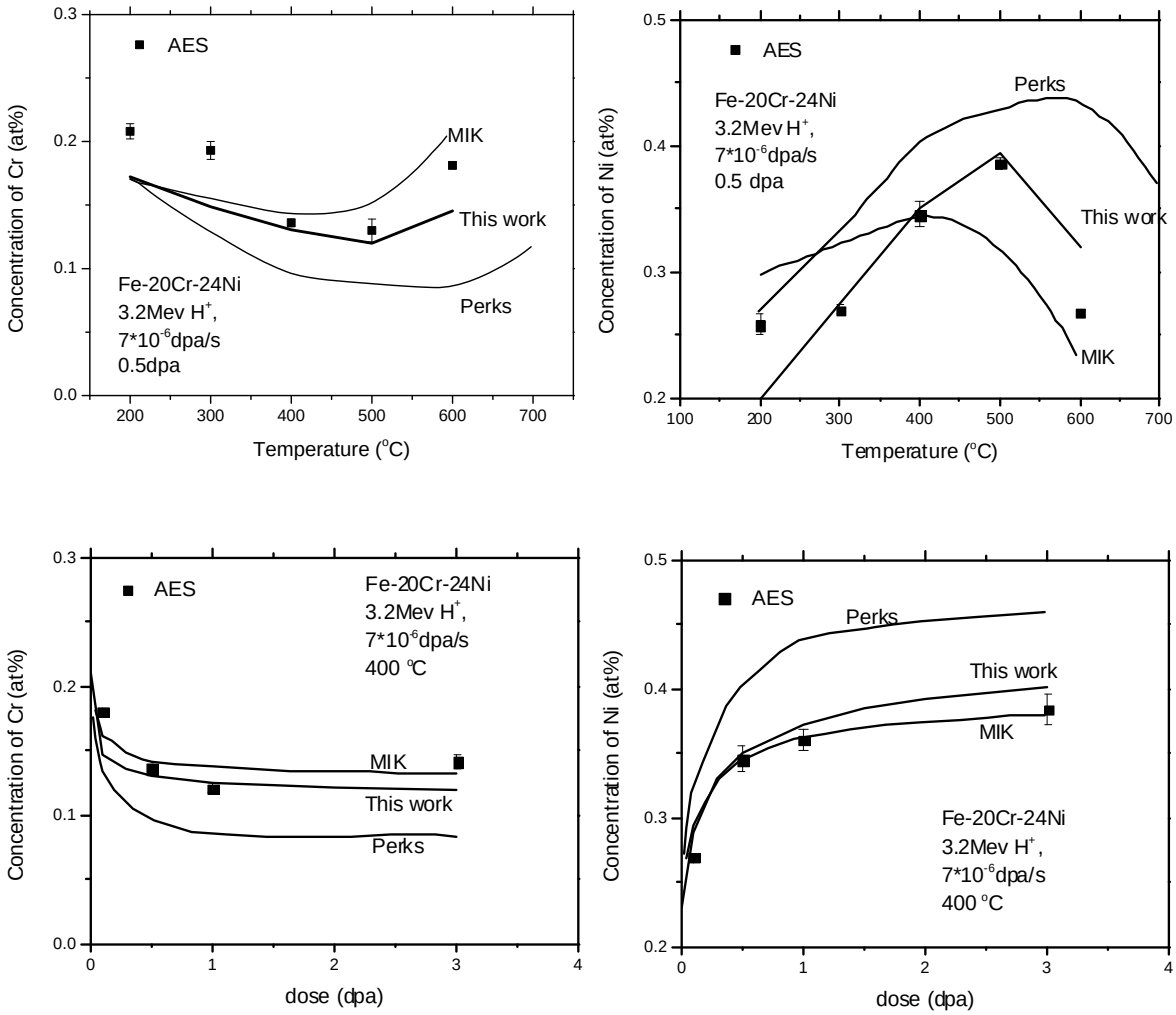

Figure 13 Calculated grain boundary concentrations for Ni and Cr as a function of temperature and dose in Fe-20Cr-24Ni (at%) alloy. Thick line denotes the results from this work and thin line the results from the MIK and Perks model [19]. Symbol denotes the AES measurements [19]

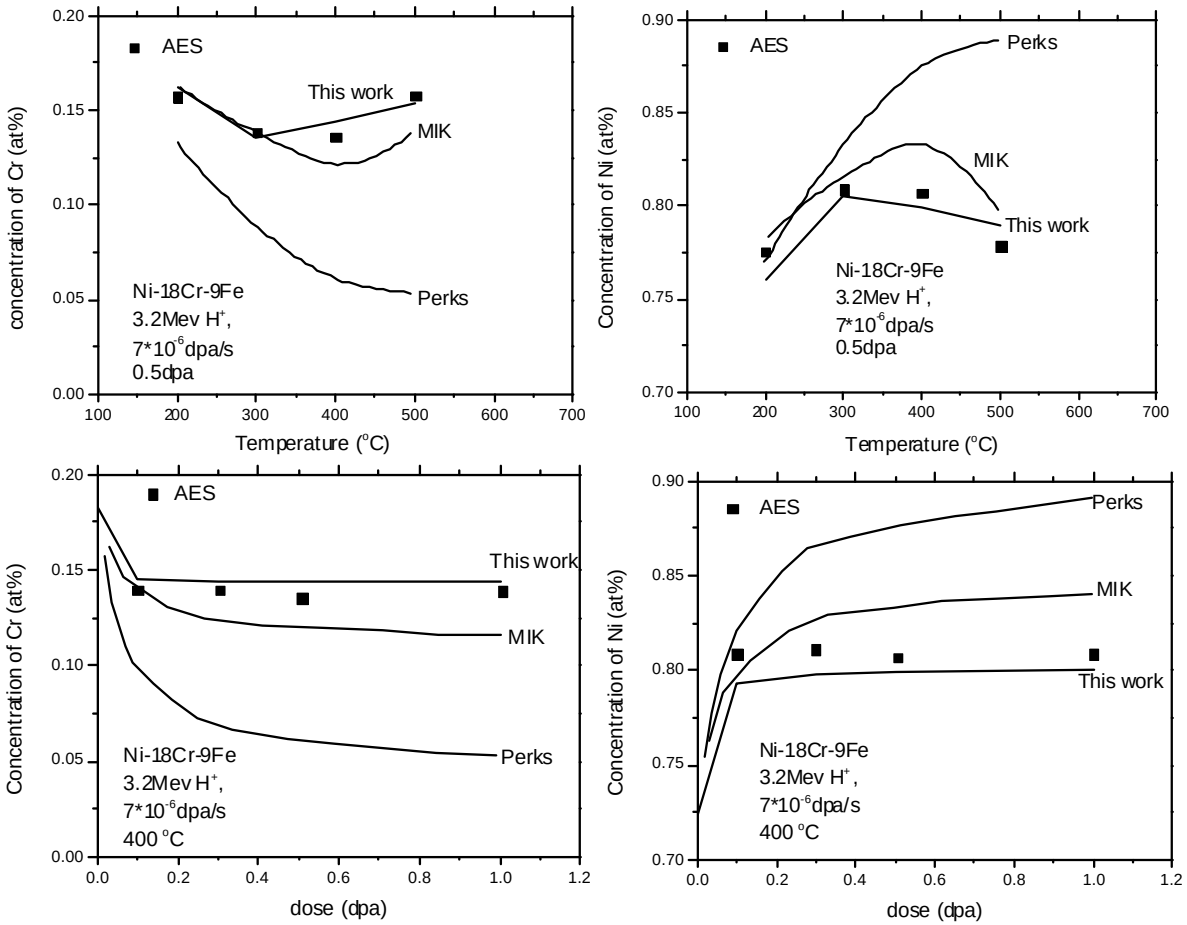

Figure 14 Calculated grain boundary concentrations for Ni and Cr as a function of temperature and dose in Ni-18Cr-9Ni (at%) alloy. Thick lines denote the results from this work and thin lines the results from the MIK and Perks model [19]. Symbol denotes the AES measurements [19]